Delivery efficiency for large mobile targets

Master's Thesis

Samuel Kurucz

samuel.kurucz@proton.me

Paul Scherrer Institute
University of Zurich

Supervisors:
Dr. Jan Hrbacek, Prof. Dr. Anthony Lomax
Prof. Dr. Jan Unkelbach

January 16, 2023

Acknowledgments

I would like to thank, first and foremost, Dr. Jan Hrbacek for his help, support, and patience during the duration of this project. His guidance and input have been of the highest value.

External collaborator Steven van de Water who developed the spot reduction algorithm has helped with many technical issues arising from the application of the script on the types of cases that have never yet been tried; without him, this thesis would not be possible.

Claudio De Angelis was the one who helped me with any issues regarding the in-house developed TPS PSIplan, showed me all the inner workings of PSI systems, and guided me through various SOPs.

My gratitude also goes to Prof. Dr. Anthony Lomax for giving me the opportunity to do this project at Paul Scherrer's Institute and for providing all the necessary tools and equipment to complete this thesis.

Special thanks are owed to Dr. Vivek Maradia for all the introduction to the procedures and inner workings of the Center for Proton Therapy at PSI.

Prof. Dr. Jan Unkelbach provided the necessary connection between the University of Zurich and PSI; without that, this project would also not have been possible.

Eigenständigkeitsvereinbarung

Hiermit erkläre ich, dass ich die vorliegende schriftliche Arbeit selbstständig und nur unter Zuhilfenahme der in den Verzeichnissen oder in den Anmerkungen genannten Quellen angefertigt habe. Ich versichere zudem, diese Arbeit nicht bereits anderweitig als Leistungsnachweis verwendet zu haben. Eine Überprüfung der Arbeit auf Plagiate unter Einsatz entsprechender Software darf vorgenommen werden.

Declaration of Originality

I hereby declare that the thesis with title
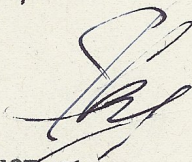
Delivery efficiency for large mobile targets

has been composed by myself independently and only with the aid referred to in References/Bibliography and that no means other than those declared were used.

In every single case, I have marked parts that were taken out of published or unpublished work, either verbatim or in a paraphrased manner, as such through a quotation.

This thesis has not been handed in or published before in the same or similar form. A review of the work for plagiarism using appropriate software may be made.

Košice, SLOVAKIA
01/09/2022

Full name: Samuel Kurucz

Matriculation number: 20-744-413

Abstract

We looked at four cancer patients treated at the Center for Proton Therapy at Paul Scherrer's Institute. Treatment plans that were used for the treatment of these patients were used as the input for the spot reduction optimizer algorithm created by Steven van de Water. The two sets of plans, the original treatment plans and the newly created spot-reduced plans, were analyzed to ascertain the benefits and disadvantages of such an approach.

Spot reduction of up to 94.8% was achieved for one patient. The correlation of the spot reduction with the delivery time and the fulfillment of prescribed clinical goals was analyzed.

The procedures used in this work can be utilized for more robust studies and for finding common features and conditions for the most optimal combination of spot reduction, delivery time, and completion of the prescribed clinical goals.

Contents

Introduction

Proton radiotherapy has gradually gained popularity since being introduced in 1954 at Berkley, California [1]. With that, maximizing dose delivery efficiency is one of the essential objectives in this field. Excluding the cost of the treatment, one of the significant challenges is the time (in)efficiency of Intensity Modulated Proton Therapy (IMPT) on targets that are large or complex [2].

Delivery time is of concern for both the passive scattering as well as the active scattering of the proton beams. In the case of active scattering, the most time-consuming process is the change of the proton beam energy, while for passive scattering, it is the manual installation of the compensators and/or collimators.

The delivery time might be reduced by using spot reduction optimization. This optimization should not compromise clinical goals set by an MD, or at least the completion of the clinical goals should be comparable to the clinically approved plans used for treating the patients analyzed in this work.

1.1 Protons

Protons, being charged particles, interact with matter very differently than photons. While for the photons, the most likely scenario when traveling through the human body (water) is that there is no interaction at all for clinically used energies, and the photon simply traverses the body; protons behave differently.

$$-\left\langle \frac{dE}{dx} \right\rangle = \frac{4\pi}{m_e c^2} \frac{nz^2}{\beta^2} \left(\frac{e^2}{4\pi\varepsilon_0} \right)^2 \left[\ln \frac{2m_e c^2 \beta^2}{I(1-\beta^2)} - \beta^2 \right] \tag{1.1}$$

Where v is the speed of the particle, z is the particle charge, E is the particle energy, I is the mean excitation energy of the material, n is the electron density of the material, c is the speed of light, ε_0 is the vacuum permittivity, $\beta = \dfrac{v}{c}$, e and m_e the electron charge and rest mass respectively.

Protons behave according to the Bethe-Bloch equation 1.1, i.e., their energy loss is inversely proportional to their velocity squared [3]. Protons have a finite range in the patient according to this relation. This is also the reason why protons at the end of their track exhibit what is called a Bragg peak [3]. The position of said Bragg peak corresponds to the maximum dose delivered.
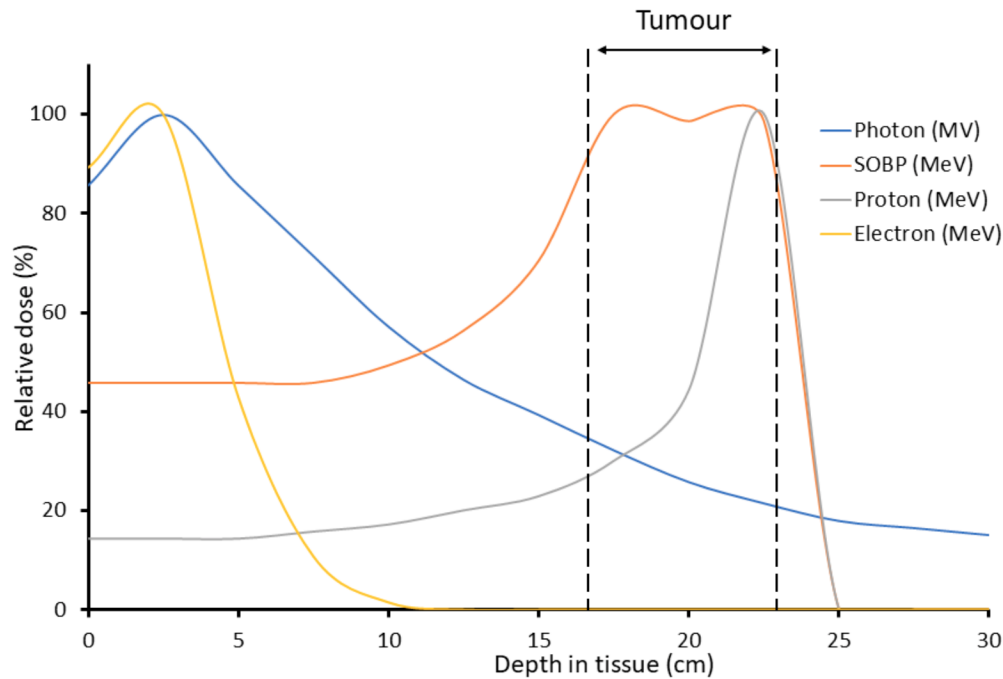
Figure 1.1: Comparison of depth-dose distributions of photons, electrons, and protons (single Bragg peak and spread-out Bragg peak - SOBP). Taken from *Hughes et al., 2020* [4].

In figure 1.1, we can see that after the Bragg peak, protons are left with very little energy, and the dose fall-off is very steep in this region. Compared to photon radiotherapy, the sparing of the distal tissue is improved drastically. So a proton beam with a set given energy penetrates the tissue up to a certain depth (that depends on said energy) and then stops.

Regarding photons, there is always a residual dose, even in the distal tissue, caused by the behavior of photons in human tissue (water) according to the Beer-Lamber law [5].

1.1.1   Proton interaction with matter

There are different interactions that the proton undergoes during its travel through the tissue. There are Coulomb interactions, either with atomic electrons or with atomic nuclei. Then there are nuclear interactions with atomic nuclei, and lastly, there is also Brehmsstrahlung. However, the probability that a particle undergoes the Brehmsstrahlung interaction is inversely proportional to the square of its mass. So Brehmsstrahlung for protons is more than a million times less likely compared to electrons.

Coulomb interactions of protons with atomic electrons

Proton along its track is most likely to interact with atomic electrons. It does so by knocking them out of the atom and therefore ionizing the atom. This ionization is what can lead to biological damage, even cell death. Furthermore, after the initial interaction, both the incident proton as well as the knocked-out electron can induce further ionizations and undergo more interactions.

As the difference in mass between the incident proton and receiving electron is great, the proton loses very little energy undergoing multiple ionizations, and its direction of motion changes very little as well.

Coulomb interactions of protons with atomic nuclei

Proton can also undergo an interaction with the atomic nucleus. It does so by deflecting on the nucleus much more compared to electrons. However, even during this interaction, the proton loses very little energy. During its path, the proton interacts with many nuclei, statistically summing up the path deviation to what is called a multiple Coulomb scattering.

Nuclear interactions of protons with atomic nuclei

Another less likely interaction is the proton splitting up the atomic nucleus into multiple fragments. These fragments can also induce ionizations in the tissue, and they vary in energy and mass depending on the energy of the incident proton.

1.1.2 Dose delivery

There are two ways of achieving acceptable target coverage, i.e., spreading out the initial few-millimeters-wide beam to cover a three-dimensional target.

Passive scattering

To achieve the lateral spread of the target passive scattering technique uses scattering foils and collimators. To adjust the locations and weights of different Bragg peaks, a range-shifter wheel can be used [6]. Passive scattering takes advantage of using patient-specific compensators that are typically produced from tissue-equivalent material. This way, the conformality of the distal edge of the target can be accomplished. Using this technique, however, the sparing of the proximal tissue can be an issue.

Active scanning

The active scanning technique, or pencil-beam scanning, uses magnets to scan the target volume. The distal edge coverage can be achieved either by changing the energy of the protons or by using range shifter material. This way, the proximally located tissue can be spared. During the delivery of a narrow pencil beam, only a very small region in the body is irradiated, the so-called spot. One spot is defined by its energy (depth), weight (number of protons), and by its position perpendicular to the beam direction. Pencil beam scanning can, in addition, also be used for intensity-modulated proton therapy (IMPT).
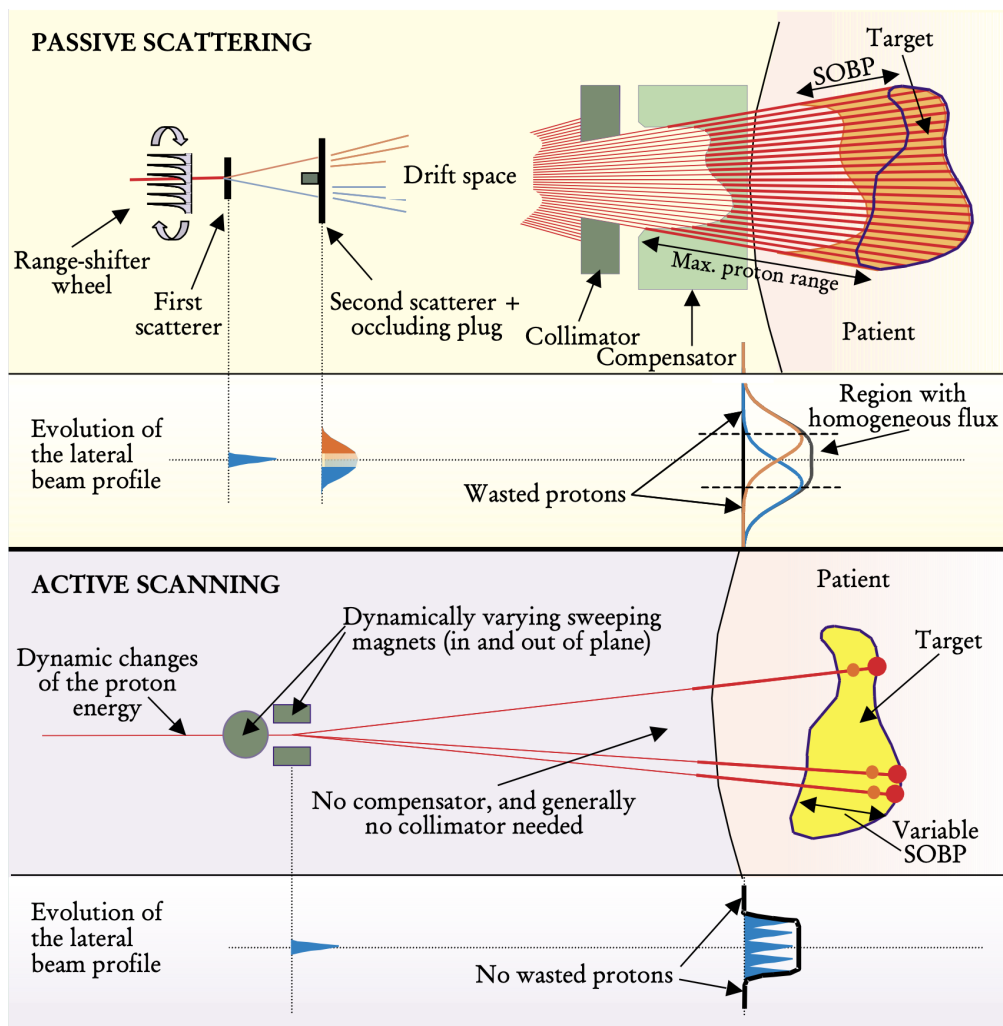

Figure 1.2: Different types of proton dose delivery. Taken from *Gotein et al., 2002* [7].

Figure 1.2 shows that using the active scattering method, there is a significant reduction in the number of wasted protons compared to the passive scanning method.

1.1.3 Linear energy transfer

Linear energy transfer or LET is defined as the amount of energy transferred by an ionizing particle to the material per distance traveled by the particle. As we can see in the 1.1, any charged particle deposits the maximum energy towards the end of its path. This would correlate to the LET values being the highest, also near the end of the particle's track, as we can see in the 1.3.

The units used in practice for LET are kilo electronvolts per micrometer $[keV/\mu m]$ or mega electronvolts per centimeter $[MeV/cm]$.
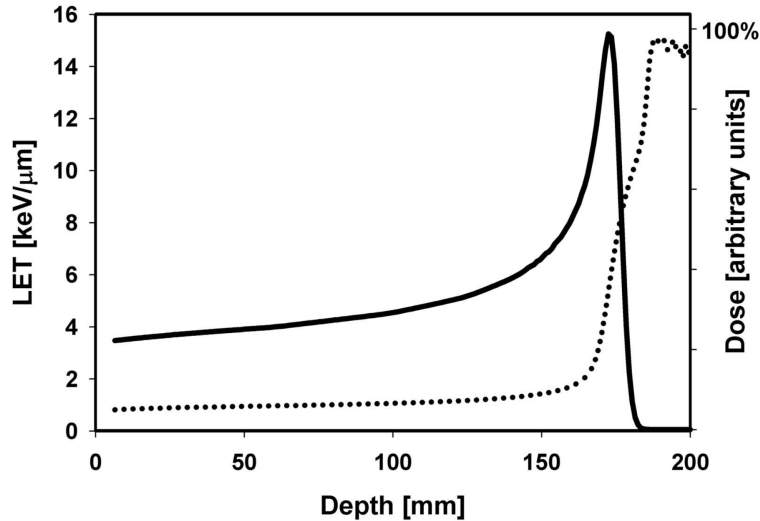

Figure 1.3: Dose (solid) and dose-averaged LET (dotted) as a function of depth in a water phantom for a 160 MeV beam. Taken from *Paganetti, 2018* [8].

It is one of the interesting questions in proton radiotherapy whether to consider LET as a factor in the optimization of the plan. It has been proven that the higher range LET values for protons relate to relative biological effectiveness or RBE values much higher than the conventionally used value of $RBE = 1.1$. [8]

These higher LET values are found at the distal edge of the Bragg peak, where the gradient of the depth-dose curve is high. This can lead to undesired effects when the tumor's distal edge is close to a critical organ, i.e., the spine.

Although the higher LET values correlate to higher RBE values, the dose delivered by these distal spots is usually smaller and, therefore, may be considered insignificant even with the higher RBE value that it carries.

Currently, it is not uncommon to find distal spot optimization features in commercial treatment planning systems (TPS) that can reduce the weights (i.e., the absolute number of protons in one spot) of the most distal spots.

It is a point of discussion in the community whether the effects are so significant that they warrant a specific indicator to be included in the optimization. [9]

1.2 Patient motion

When it comes to treating a patient with protons or with any type of radiotherapy, the motion needs to be thoroughly considered. We distinguish between interfractional and intrafractional motion. The former represents the changes in motion between different treatment sessions, while the latter corresponds to the motion changes during imaging or treatment session.

Relatively speaking, motion uncertainties combined with individual margin increments on the tumor volume have the greatest impact when it comes to treating small mobile targets [10]. In this thesis, we looked at patients with large (between 1500 and 2000 ccm target volume) mobile targets, mainly in or near the lungs and/or the liver.

Amongst the undesired effects when it comes to dealing with motion are so-called interplay effects [11]. Interplay effects take place when there is a difference between the radiation delivery timeline and the tumor motion timeline (e.g., due to breathing). These effects can result in particular spots being delivered outside of the target, which can result in target under dosage and, in turn, overdosage in healthy tissue.

1.2.1 Target delineation

During the treatment planning, one has to delineate the tumor. There are different target volumes that can be specified.

1. Gross tumor volume (GTV) is the visible tumor region on pre-treatment imaging.

2. Clinical tumor volume (CTV) is formed by incrementing the GTV by an expected microscopic spread of the tumor.

3. Internal target volume (ITV) also takes into consideration the motion of the patient's anatomy, again increasing the CTV volume.

4. Planning target volume (PTV) also considers the setup uncertainties and daily variations in patient positioning.
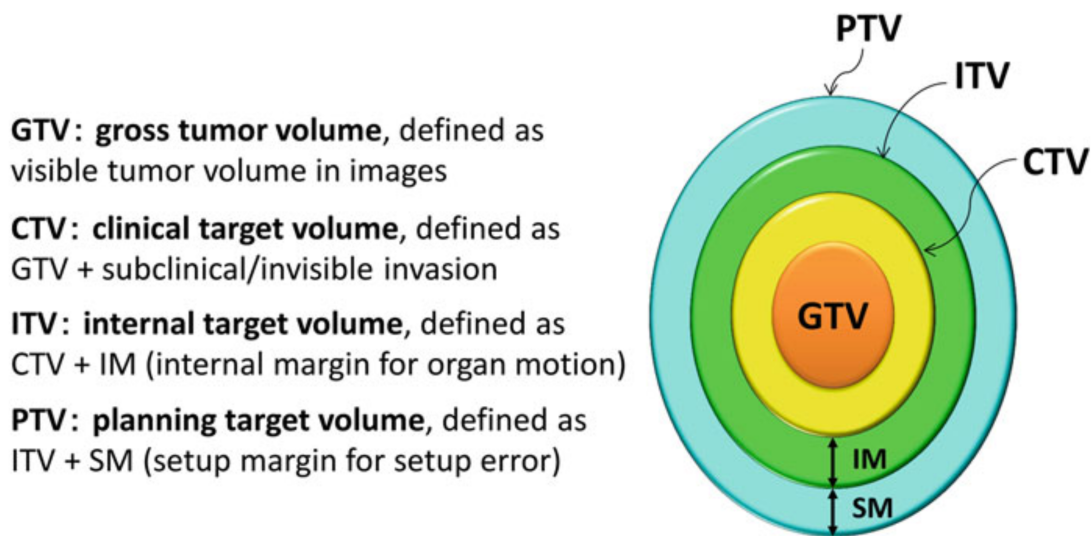
GTV: **gross tumor volume**, defined as visible tumor volume in images

CTV: **clinical target volume**, defined as GTV + subclinical/invisible invasion

ITV: **internal target volume**, defined as CTV + IM (internal margin for organ motion)

PTV: **planning target volume**, defined as ITV + SM (setup margin for setup error)

Figure 1.4: Different target volumes. Taken from *Arimura et al., 2017*[12].

1.2.2 Motion mitigation

To statistically average out any motion uncertainties (either related to the movement of the patient's anatomy or the setup uncertainty), repainting or rescanning can be used. Rescanning is the process of delivering a partial dose multiple times, together adding up to the total planned dose. Rescanning can be used to average out interplay effects.

Rescanning

We distinguish between volumetric and layered rescanning. With scaled volumetric scanning, the dose delivered during one full volume scan is equal to 1/N of the prescribed dose, where N is the number of rescans. An alternative approach, which is expected to be especially advantageous for slower systems, is called layered rescanning. It first delivers all N rescans within one' energy plane' before switching to the next plane. [13]

Gating

Another technique that can be used when dealing with mobile targets is gating. First, one needs to obtain a breathing curve of the patient. At PSI, this is done by combining multiple breathing curves of different patients to obtain a 'universal' breathing curve, which is then applied to the medical imaging (i.e., MRI, CT) of the patient in question. This results in 4DCT and/or 4DMRI for the patient. After obtaining 4D images of the patient, the gating interval and, with that, the duty cycle is to be determined.

The gating interval or gating window is the period during which the beam is on and delivering the dose. Related to that is the so-called duty cycle, which corresponds to the beam-on time over the period of the cycle. A duty cycle of 100% corresponds to the beam being on for the whole breathing cycle. At PSI, the usual clinical practice is a 30 % duty cycle. The dose is delivered in the region surrounding the full exhale point (0 % of the amplitude) on the breathing curve, specifically 30% of the breathing cycle amplitude, see figure 1.5.

Other motion mitigation techniques include breath-hold, the dose is delivered while the patient holds their breath, and tracking, the target is being tracked live during the beam-on time; however, this technique is technically challenging.
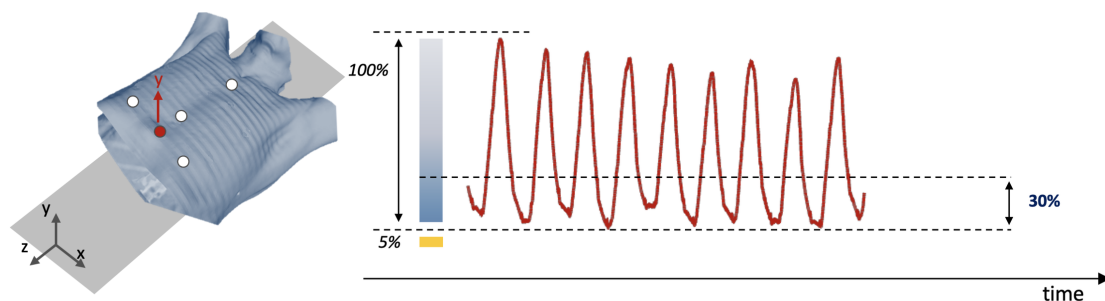

Figure 1.5: Breathing curve with 30% duty cycle. Taken from PSI presentation.

1.3   IMPT optimization

In contrast to Three Dimensional conformal Radiation Therapy (3DCRT), which is a process of forward planning, the Intensity Modulated Radiation Therapy (IMRT) uses an inverse planning approach. In the 3DCRT's case, the planner optimizes the plan by hand by changing different field parameters. This 'trial and error' approach heavily depends on the planner's experience and skills.

On the other hand, there is IMRT, which also comprises Intensity Modulated Proton Therapy (IMPT). The IMRT and, with it, the IMPT is an inverse treatment planning approach. That means that as a first step, an ideal solution of the dose distribution is provided as an input, and then the optimizer tries to find and optimize the field parameters to achieve this solution. One of the most often used approaches in IMRT is based on the minimization of a cost function that includes the objectives for the target

as well as the constraints for organs at risk.

IMPT fields deliver nonuniform dose distribution. Whereas IMRT for photons consists of using 2D fluence maps for different angles of irradiation, the IMPT uses a separate fluence map for every energy layer of the treatment plan. A fluence map can be described as a set of spot weight distributions (i.e., the number of protons in a proton beam). Optimization consists of changing said spot weights to complete clinical goals defined by the radiation oncologist. Mathematically this corresponds to constructing an objective function, which includes these clinical goals (either an objective we wish to fulfill or get close to or a constraint we are not willing to compromise on) and minimizing this objective function.

For the plans included in this study, there were to IMPT optimization methods used. For clinical plans created at PSI, the Limited-memory Broyden-Fletcher-Goldfarb-Shanno or L-BFGS optimization algorithm was used. It is an iterative algorithm based on a quasi-Newtonian optimization method.

For spot-reduced plans, the optimizer used a prioritized or exact optimization. This method consists of defining priorities for different prescribed clinical objectives and constraints. The change in the optimization method is due to the underlying nature and technical aspect of the spot reduction algorithm used for this study.

1.4 Aim of the project

It has been proven that spot reduction optimization provides a significant reduction in delivery time (46% reduction) without necessarily compromising the plan quality [14]. However, this study was done for a head-and-neck cancer patient with a PTV of 293 cm^3. Our project studies patients with lung and/or liver tumors with PTVs that are significantly larger, with the smallest tumor volume being $1\,207$ cm^3.

By applying spot reduction optimization to clinical treatment plans for these patients, we aim to prove that spot reduction optimization can result in a significant reduction in delivery time and the number of spots. The plan quality of spot-reduced plans might be worse than that of clinical plans. This effect might arise due to the large volume of the target and the underlying nature of spot reduction.

The purpose of this thesis is to compare the resulting plans from two different types of optimization methods, more specifically to assess if the reduction in delivery time of the spot-reduced plan is worth the possible reduction in the plan quality (most often the target coverage). A different optimization method is required due to the nature of the developed spot reduction algorithm used in this study. The workings of the algorithm are explained to an extent, but it is not the significant focus of the work.

In this work, the term clinical plans is used for simplicity, and it refers to the clinically approved plans at PSI that were used for treatment.

Methods and Materials

2.1 Patient data

2.1.1 4DCT

To perform gated radiotherapy, it is necessary to have a time-resolved imaging method of the patient's anatomy and its density. In the case of computed tomography (CT) imaging technique, adding the time resolution to a three-dimensional CT (3DCT) gives rise to what is referred to as a four-dimensional CT (4DCT). [15]

Such a CT is obtained by acquiring a series of 3DCT images at different phases of the patient's breathing cycle. Along with this also patient's breathing cycle is recorded. This is done at PSI using the optical tracking system that records the patient's breathing curve. The breathing curve illustrates the patient's breathing cycle as a sinusoid function, with the peak amplitude representing the full-inhale cycle phase and zero level amplitude consequently representing the full-exhale cycle phase. [16]
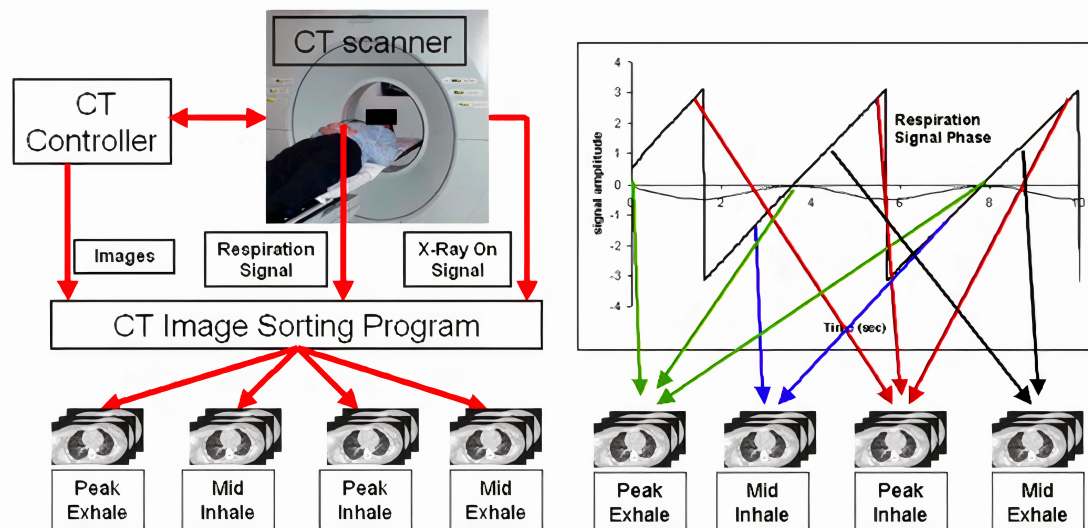

Figure 2.1: 4DCT phase acquisition related to the patient's breathing cycle. Taken from *Vedam et al., 2002* [15].

The CT is obtained in eight phases at PSI, as the figure above shows. [15]. Naturally, this does not fully represent the patient's anatomy during the complete breathing cycle,

and the patient's density distributions between the eight phases have to be interpolated with the use of the breathing curve. The reproducibility issue between different breathing cycles of a patient has to be considered. [17]

4DCT, however, helps significantly with minimizing motion artifacts compared to 3DCT, where breathing motion is not considered. Therefore, contouring difficulties can arise with anatomical distortions caused by motion artifacts. It has been shown that by taking motion into consideration, the target volume margins can be significantly reduced [17]. More precise contouring and smaller margins can achieve more clinical goals with higher quality.

Deformable image registration

Motion information between phases is quantified by deformable image registration (DIR). The DIR calculation process is as follows; one image has to be set as a reference (this is usually the exhale phase image), then another image is set as the moving image. DIR then calculates geometric differences induced by motion between the two image phases.

This results in deformation vector fields, or DVFs, representing how each voxel moves in time with every phase.

For the purposes of 4D dose calculation, DVFs are extracted from 4DCT using a DIR algorithm based on B-splines [18] using open-source software, 'plastimatch' [*plastimatch, http://plastimatch.org*]. [16]

2.2 Treatment planning

The clinical treatment plan is generated using PSI's own proprietary treatment planning system - PSIplan [19, 20]. The user-defined composite objective function optimization used in PSIplan is based on the quasi-Newton method, and optimal weights for a set of candidate proton spots are obtained [21].

The composite objective function is formed by combining weighted quadratic objectives for each treatment planning goal [14]. Adjusting the weighting factors of these objectives generates a treatment plan using a trial-and-error approach.

Given the right starting conditions, the system aims intrinsically at a homogeneous target dose for each field. This is due to a damping term included in the optimization. The minimum spot weight limit is set to approximately 0.05 Giga-protons. Spot weights below this limit are set to zero during each optimization iteration. [14]

2.3 Spot placement

By default, the PSI's treatment planning system, PSIplan, distributes the spots in a $4x4mm$ rectangular grid, but for these large targets, a $5x5mm$ grid was used. The spacing of the energy layers depends on the energy of the beam; under $100MeV$ energies of the beam, the spacing of the energy layers is $2.5mm$. Over $100MeV$ energies of the beam, the spacing of the energy layers is $5mm$.

The lateral profile of the spots is defined by the Gaussian distribution:

$$f(x) = \frac{1}{\sigma\sqrt{2\pi}}e^{-\frac{1}{2}(\frac{x-\mu}{\sigma})^2} \qquad (2.1)$$

The full width at half maximum (FWHM) can be used to describe the width of the spot. For the Gaussian distribution, the FWHM calculation can be approximated to:

$$FWHM \approx 2.355\sigma \qquad (2.2)$$

The spot sizes used at PSI have a sigma of $6-7mm$, so the width of the spots is roughly $14-17mm$.

2.4 Spot reduction algorithm

The spot reduction algorithm used in this study is based on the iterative pencil beam resampling technique [14]. This technique involves repeated inverse optimization of the sampled candidate spots while adding a small sample of randomly selected spots in each iteration and subsequently excluding low-weighted ones until plan quality deteriorates. Spot-reduced plans manifest higher-weighted spots that are more sparsely distributed compared to the clinical IMPT plans.

Each iteration of the algorithm consists of the following steps:

1. Random selection of a relatively small number of candidate spots

2. Dose matrix calculation and inverse optimization

3. Spot reduction

4. Adding a randomly selected subset of different candidate spots to the already existing solution (achieved after point 3)

Using this approach, it is ensured that all subsequent solutions are improvements of existing ones. After each iteration, there is a distribution of spot weights achieved that fulfills some of the objectives but does not fulfill others. In a subsequent iteration, by adding another subset of randomly selected candidate spots and optimizing already

existing spots together with newly selected candidate spots, a different distribution of spot weights is achieved, which improves the solution, and this process is aimed to fulfill the objectives that have not been fulfilled in previous iterations.

As the objectives and constraints for different targets and OARs are defined to mimic the clinical plan (and in the clinical plan, these were defined by an MD), the only parameters a user can adjust are the priority levels of these objectives and constraints and the sample size of spots considered in the randomly selected subset. However, the adjustment of these parameters is not the scope of this work.

As a rule, the target objectives were always defined with the highest possible priority, with secondary target dose parameters such as variance and square deviation having lower priority. Then OARs objectives and constraints were given priorities lower than that of the target.

2.4.1 Dose optimization

Dose optimization was performed using a prioritized (or lexicographic) approach, in which the user can define constraints (that have to be fulfilled) and objectives with a certain priority. The objectives are divided into different priority levels. A composite objective function is constructed from these objectives within the given priority level and then optimized. Previously achieved objectives with higher priority are set as constraints for the following optimization of lower priority objectives.

2.4.2 Spot reduction

This step in the algorithm consists of excluding low-weighted spots (i.e., spots below a minimum spot weight of 0.001 Giga-protons and/or the spots responsible for the lowest 0.5% of spot weights) and reoptimization of weights of remaining spots while constraining all previously achieved dose parameters. This process is repeated until any further spot exclusion results in a violation of these constraints.

In this study, we used a total sample size of 12,500 candidate spots for all fields per iteration. This sample size was the same for all four patients.

Resampling iterations were terminated when none of the target and OAR objectives improved by more than 3%. The machine setup (i.e., field arrangements, pre-absorber, initial spot grid spacing, and the beam model for PSI Gantry 2) was identical to the one used for clinical plans.

After plan generation, the spot-reduced plan was imported back into PSI's proprietary TPS PSIplan for 4D dose calculation and machine steering file generation. This was done using a custom PSI script that produces dose distribution files for each field from the spotlist files.

The flowchart of the spot reduction treatment planning compared to the conventional treatment planning can be seen in 2.2.

Conventional treatment planning:
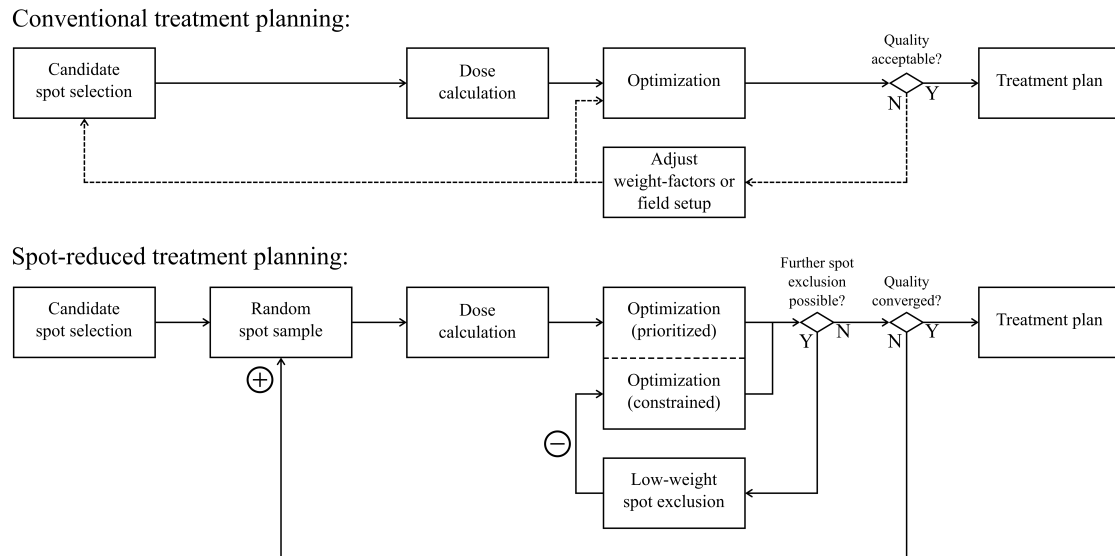
Spot-reduced treatment planning:

Figure 2.2: Flow charts of the optimization process, comparing conventional treatment planning (top) and spot-reduced treatment planning (bottom). Taken from *van de Water et al., 2020* [14].

2.5   4D dose calculation

After achieving an acceptable spot-reduced plan, the 4D dose calculation is necessary to get time stamps of individual spots and essentially to evaluate the duration of the dose delivery with respect to motion (breathing).

There are various algorithms that can be used for 4D dose calculation. One of the earliest algorithms was described by *Rietzel et al.* [22]. It consists of static dose distribution calculation for every phase of a 4DCT and averaging out the resulting distributions. This method assumes that the dose can be delivered homogeneously to all the CT phases, which is not feasible using pencil beam scanning. [23]

At PSI, an in-house developed algorithm [23] is used for 4D dose calculation. It is based on deforming grid approach and the ray casting beam model [24]. By applying this

algorithm, the regular grid is deformed according to the breathing cycle of the patient. Furthermore, the algorithm takes into account the density changes in different breathing phases.

To achieve the 4D dose distribution, the original set of defining parameters of a spot (i.e., energy, spot position, spot weight) is expanded by the time stamp of a spot. This is calculated in the PSI 3D treatment planning system - PSIplan.

The information from the 3D dose distribution is taken; spot positions and spot weights. This information is then converted to machine-readable steering files by the steering file generator (*SFGen*). The 3D dose is then delivered, and during the delivery, the dose distribution in one specific water equivalent depth is measured, and the actual spot positions, weights, and time stamps are logged. These delivery log files are then coupled with the optical motion tracking system with in-house developed tools. From that, the 4D dose distribution is calculated. The individual steps are visualized in 2.3.
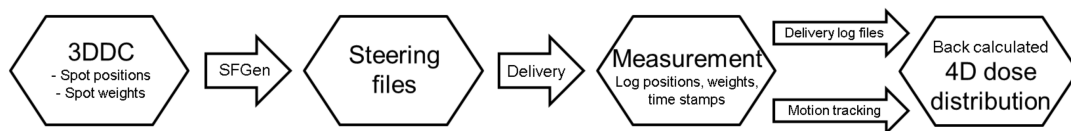

Figure 2.3: 4DDC Flowchart. Taken from *Krieger et al., 2018* [23]

2.5.1 Grid deformation

4D dose calculation used at PSI is based on dose calculation grid deformation to model the patient's motion. [23]

For this purpose, deformable image registration is used to estimate the motion fields between each phase of the 4DCT and the reference CT (usually, the 0% inhale phase is used) [23].

The dose calculation grid is then deformed accordingly as a function of time. Using a deformed grid, it is computationally efficient to interpolate this function to any interval; therefore, the original temporal resolution of the 4D imaging can be improved. This 4D dose calculation algorithm operates at a millisecond level. [23]
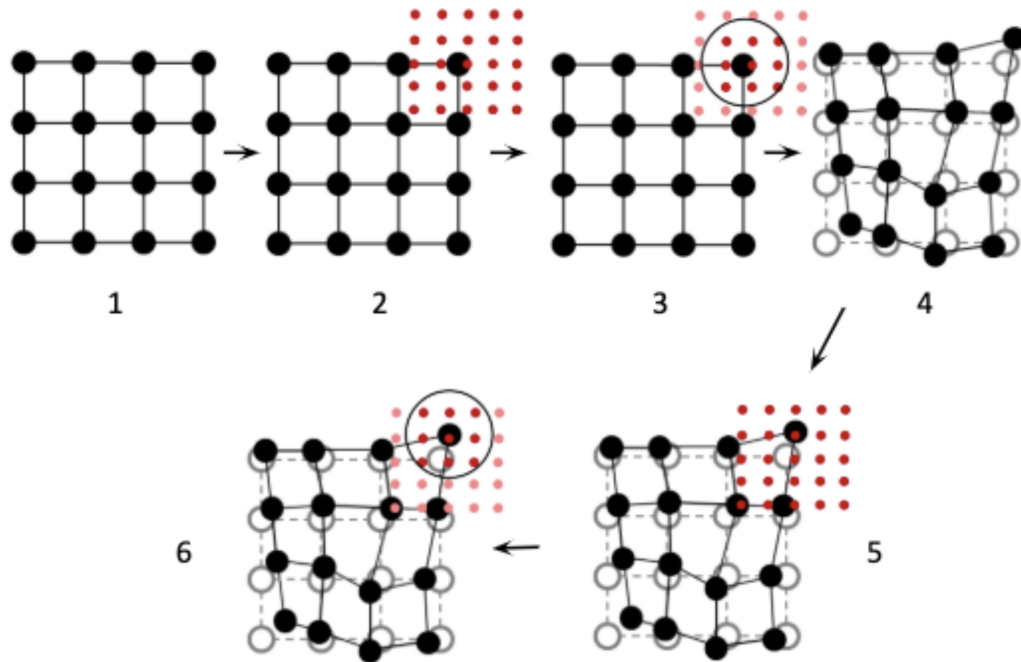
Figure 2.4: Grid deformation steps: 1. A dose grid that covers a volume of interest in the patient geometry is created; 2. All spot positions (red points) are calculated; 3. The dose contribution for each pencil beam at all affected dose grid points is calculated by ray casting algorithm; 4. With motion vector fields, the dose grid is deformed as a function of time; 5 & 6. 4D dose distributions are obtained. Taken from *Pauline Novak's MSc. Thesis, 2020* [16]

2.5.2   Ray casting beam model

The human body essentially consists of three types of medium: water, air, and bone. Along the track of the proton, it is these three mediums and their eventual superposition of these that are taken into account when adjusting the range of the beam for density changes.

Neglecting density variations across the pencil beam can lead to errors in the dose distributions. Especially when the pencil beam is large, which the one used at PSI is ($\sigma = 6 - 8mm$). [24]

The scanned pencil beam model uses a physical pencil beam model based on measurements of the physical pencil beam in water and air. [24]

Building upon this model is the elemental pencil beam model, which is fundamentally the same as the scanned pencil beam model, but it uses an infinitesimally small phase space to model the pencil beams. Applied physical pencil beams are then a result of the superposition of these elemental pencil beams. [24]

These models do not realistically represent what happens to the pencil beam when it passes through a heterogeneous artifact within a more-or-less homogeneous medium. In figure 2.5, we can see that the inserted high-density slab is not at all modeled in the scanned pencil beam model, but the effects of the presence of the slab are clearly visible when using Monte Carlo simulations to model the pencil beam.

Ray casting beam model is computationally more time efficient than using Monte Carlo simulations to model pencil beams. Using the ray casting technique, the original depth-dose distribution from the physical scanned beam model is scaled by the projected water-equivalent range of each dose grid spot. The energy loss variation of the protons is modeled as a parallel projection of the density. The ray casting technique is only valid for a parallel beam with a small angular divergence, like the one used at PSI [24]. This model neglects multiple Coulomb scattering of the protons, which results in Bragg peak degradation.
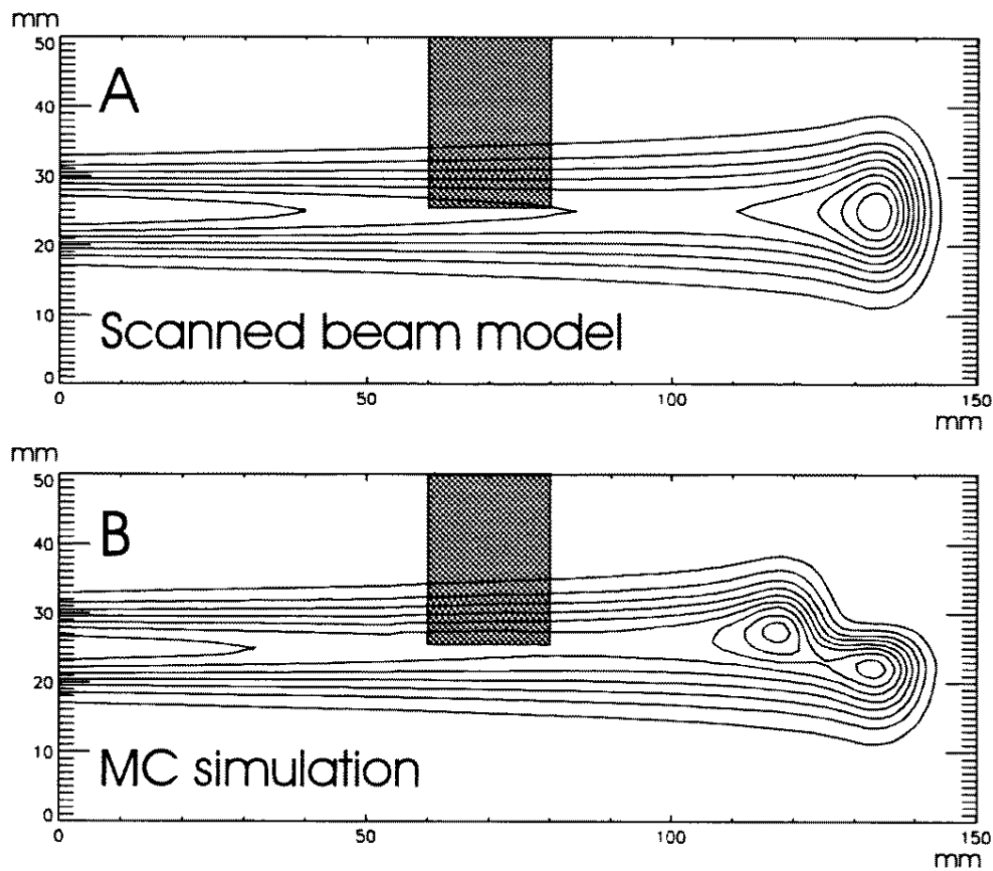
Figure 2.5: Visualization of differences between the pencil beam model and the Monte Carlo simulation model. Taken from *Schaffner et al., 1999* [24]

2.5.3 LET_D distribution calculation

A 3D dose-averaged LET distribution was independently calculated by an in-house script developed for this purpose.

LET_D distribution calculation for static plans, both clinical and spot-reduced, was performed. This 3D distribution was then visualized at a specific transaxial CT slice.

For simplicity, the term LET distribution used in this work refers to the dose-averaged LET distribution.

2.6   Delivery times

As the spot-reduced plans considered in this study have not been actually delivered, the delivery times of these plans are an approximation. To approximate the delivery times of the plans, at PSI, there is a custom script called *timingLibrary* that estimates the delivery times based on the dose distribution of the plan and parameters specific to the hardware used for the treatment. These delivery time estimates are usually lower than the actual delivery time, but as the same script was applied to all plans, the comparative value of these estimates is sufficient.

The duration of the delivery of one spot consists of a dead time to prepare and tune the spot, then there is the time needed for the sweeper magnets to move the pencil beam to the correct location for the delivery, and then there is the time needed for the actual delivery of the spot. The sweeping magnet time is different for the x-axis (U-coordinate in the coordinate system of the machine) and for the y-axis (T-coordinate in the coordinate system of the machine). For the x-axis, it can be approximated to 0.5 cm/ms, and for the y-axis, it is approximately 2.2 cm/ms.

The delivery of the spot (t_{spot}) depends on the weight of the spot. This component is affected by the spot reduction, and it scales linearly with the number of monitor units (MU), which represents the spot weight.

$$t_{spot}[ms] = MU * 3.3333 * 10^{-3} \tag{2.3}$$

Where the slope $3.3333 * 10^{-3}$ has the units of ms/MU.

The delivery time of one energy layer depends on the number of spots within the energy layer and the delivery time of these spots. There is also the control system dead time between elements, that is, the time between the end of one element and the start of its following element, where the treatment control system (TCS) is processing information about the spot. This component amounts to 2.25 ms.

The dead time component increases with the number of spots, so overall, as the spot-reduced plans have significantly lower spots, the total dead time is lower. However, the beam-on time for a single spot is usually higher for the spot-reduced plans, as the spots have increased spot weights that are proportional to the number of monitor units, MU (see equation 2.3). Total beam-on time for both sets of plans is comparable as this increases with the spot weight (i.e., the number of protons), and the total number of protons varies very little between the clinical plans and the spot-reduced plans.

The delivery of the whole field with all the energy layers depends on the number of energy layers and the delivery time of these layers. There is also a dead time needed to switch between two energy layers. This component can be approximated to 100 ms. So, even if all the spots within one energy layer are removed by the spot reduction algorithm, the effect on the delivery time is minimal. Typically, spot-reduced plans have 10% fewer energy layers.

There is another component that is called energy ramping. This process is performed before the delivery of each field. The system will go from its current energy down to the minimum energy of $\approx 70MeV$ and then ramp up to the maximum energy of $230MeV$. From here, it will ramp down to the energy required to deliver the spots. This component can be approximated to $11s$.

2.7 Plan Evaluation and Analysis

Both sets of plans were normalized toward the mean dose of the PTV target volume, and the following metrics were used to evaluate and compare them.

2.7.1 Dose-Volume Histogram

Dose-volume histogram condenses a large amount of information about the dose and the volume into an easily interpretable graphical summary. It provides a visualization of the radiation distribution throughout the target volume and the anatomical structures of interest [25].

Generally, histograms represent a statistical distribution of data distributed into defined bins or ranges. We distinguish between a differential and a cumulative histogram. For the purposes of the data representing dose and volume, the accumulated volume of voxels receiving dose in a defined dose interval against a set of equispaced dose intervals is known as the differential dose-volume histogram.

A cumulative dose-volume histogram plots this data as the volume receiving a dose greater than or equal to a given dose against that dose over the expected dose range [25].

2.7.2 Metrics

A set of metrics was chosen to compare the quality of different plans. The choice was made on the basis of the popularity of metrics together with the results of a study done by *Kaplan et al., 2021* [26].

PTV coverage

To describe the coverage of the planned target volume (PTV), a V95 metric is used. This metric is defined as the PTV percentage receiving equal to or more than 95% of the prescribed dose. Typically V95 values of 95% or more are sufficient for the plan to be acceptable for clinical cases. However, this is not the case in this work, as the approved clinical plans often do not fulfill this requirement due to practicality.

Homogeneity

In spot-reduced plans, the dose homogeneity will suffer due to the underlying physical concept of spot reduction. To describe the dose homogeneity, two metrics were used. First, the homogeneity index as defined by Radiation Therapy Oncology Group [27]. This index is defined as follows:

$$HI_{RTOG} = \frac{D_{max}}{D_p} \tag{2.4}$$

Where D_{max} is the maximum dose to the PTV, and D_p is the prescribed dose.

This index, however, does not describe in detail the homogeneity of the dose, despite its great popularity for treatment plan analysis. The use of maximum and minimum doses is not ideal because it describes the said doses at different points rather than in volumes. The sensitivity of the maximum and minimum dose calculation to the dose-calculation parameters, such as grid size and grid placement, makes this technique less reliable [28] [29]. Generally, this index's values range between $1.00 - 1.50$ in real-world patient treatment plans, and the lower the value, the more homogeneous the plan is.

$$HI_{ICRU} = \frac{D_{2\%} - D_{98\%}}{D_{50\%}} \tag{2.5}$$

Where $D_{2\%}$ is the dose received by 2% of the PTV, $D_{98\%}$ is the dose received by 98% of the PTV, and $D_{50\%}$ is the dose received by 50% of the PTV.

Here another homogeneity index is defined. This one represents better the true minimum and maximum dose because it defines these doses in volumes rather than at points. It uses the dose that covers 2% of the PTV and the dose that covers 98% of the PTV to describe homogeneity. Here a zero-value homogeneity index indicates a nearly homogeneous dose distribution [30].

Conformity

To determine dose conformity, an adjusted conformity index was used. It is based on the conformity number from *ICRU 83* report [30]. The *ICRU 83* conformity number is defined as follows:

$$CN_{ICRU} = \frac{V_{T,ref}}{V_T} \times \frac{V_{T,ref}}{V_{ref}} \tag{2.6}$$

Where $V_{T,ref}$ is a target volume covered by a reference isodose, V_T is the volume of the target, and V_{ref} is a volume covered by a reference isodose.

An adjustment was made to create a custom conformity index (further denoted as CI_{sk}), where V_{ref} is a volume of the structures defined for the clinical goals covered by a reference isodose. So if a structure is not defined for a clinical goal, its volume is not

counted toward the V_{ref} volume, even though the reference isodose might cover some part of its volume.

As a reference isodose, the 95% of the prescribed dose isodose was chosen. Higher index values indicate more precise and conformal irradiation of the target volume.

2.7.3   Clinical goals

To assess the plan's quality, the clinical goals table is used. These goals were prescribed by a medical doctor at PSI and were used to define the objectives and constraints for the clinical plans used at PSI. The spot-reduced plans' settings and prescriptions were always set to mimic these goals from the clinical plan.

Chapter 3

Results

3.1 Patient 1

Target structure	Main target location	Volume $[cm^3]$	Prescribed dose $[Gy]$	Fraction dose $[Gy]$
PTV_07_2000	Abdomen	1638.09	20	2

Table 3.1: Patient 1 target definition and prescription

Patient 1 was diagnosed with an unspecified Hodgkin's disease, and the tumor was located in the abdomen with a volume of 1638.09 cm^3. He/she was prescribed the dose of 20 Gy to be delivered during ten fractions, with the fraction dose being 2 Gy. The target structure was contoured and named PTV_07_2000 for use in the TPS PSIplan. Figure 3.1 compares this target coverage between the two sets of plans in the PSIplan's dose distribution viewer. One can see the effects of the spot reduction in the colorwash visualization, with the dose distribution on the right being more 'grainy' (see 3.1).

For this patient, the dose was delivered with three fields. The use of the preabsorber was decided automatically by the optimizer. The specific couch and gantry angles, together with the defined nozzle extension, can be seen in table 3.2.

Field	Gantry angle [°]	Couch angle [°]	Preabsorber	Nozzle extension $[cm]$
F0	170	170	AUTO	20
F1	160	0	AUTO	20
F2	75	0	AUTO	16

Table 3.2: Patient 1 field-specific parameters

The plans considered for this patient and subsequent plan evaluation and dosimetric analysis were four clinical plans, with one static and three 4D plans, with one, two, and four rescans, respectively. The same number and type of plans were considered for the category of the spot-reduced plans.

The spot reduction achieved here was 85.1% comparing the static spot-reduced and clinical plan. With this reduction in the number of spots, a 14.8% amount of time was also saved. In seconds this equals 67.4 s saved comparing the static plans. The V95

D$_p$ = 20 Gy	Clinical				Spot-reduced			
	Static	4D			Static	4D		
Number of rescans		**1**	**2**	**4**		**1**	**2**	**4**
Number of spots	50 621				7 152			
Delivery time	454.06 s	454.06 s	628.07 s	981.86 s	386.67 s	386.67 s	505.91 s	748.03 s
Delivery time change					-14.84 %	-14.84 %	-19.45 %	-23.82 %
PTV V95%	96.04 %	90.66 %	92.47 %	94.25 %	95.60 %	88.88 %	91.26 %	94.50 %
HI$_{RTOG}$	1.11	1.36	1.30	1.17	1.10	1.42	1.29	1.18
HI$_{ICRU}$	0.021	0.091	0.081	0.048	0.020	0.118	0.097	0.047
CI$_{sk}$	0.754	0.704	0.736	0.751	0.762	0.692	0.714	0.744
PTV D2%	20.60 Gy	21.80 Gy	21.62 Gy	21.08 Gy	20.56 Gy	22.18 Gy	21.88 Gy	21.04
PTV D98%	18.70 Gy	17.84 Gy	18.08 Gy	18.32 Gy	18.40 Gy	17.12 Gy	17.86 Gy	18.14

Table 3.3: Patient 1 dose metrics and delivery times

OAR	Prescription	Static		4D	
		Clinical	Spot-reduced	Clinical 4 rescans	Spot-reduced 4 rescans
Heart	Mean dose: $2\ Gy$	$0.34\ Gy$	$0.34\ Gy$	$0.68\ Gy$	$0.64\ Gy$
Lung L	Mean dose: $5\ Gy$	$6.90\ Gy$	$6.88\ Gy$	$7.42\ Gy$	$7.30\ Gy$
	Constraint: $V20\ Gy\ <\ 20\ \%$	$5.7\ \%$	$5.9\ \%$	$6.1\ \%$	$6.8\ \%$
	Constraint: $V5\ Gy\ <\ 55\ \%$	$44.7\ \%$	$44.8\ \%$	$48.6\ \%$	$47.1\ \%$
Spinal cord	Max dose: $20\ Gy$	$16.28\ Gy$	$15.64\ Gy$	$16.38\ Gy$	$15.74\ Gy$
Pancreas	Mean dose: $15\ Gy$	$15.16\ Gy$	$15.14\ Gy$	$14.64\ Gy$	$14.68\ Gy$
	Constraint: $D2\% \ <\ 103\ \%$	$102.5\ \%$	$102.5\ \%$	$104.7\ \%$	$103.8\ \%$
Kidney L	Mean dose: $10\ Gy$	$10.36\ Gy$	$9.34\ Gy$	$10.34\ Gy$	$9.26\ Gy$
Kidney R	Mean dose: $15\ Gy$	$4.58\ Gy$	$4.10\ Gy$	$4.56\ Gy$	$4.08\ Gy$
Bowel	Constraint: $D2\% \ <\ 103\ \%$	$101.7\ \%$	$101.8\ \%$	$102.5\ \%$	$103.7\ \%$
Liver	Mean dose: $5\ Gy$	$0.42\ Gy$	$0.38\ Gy$	$0.42\ Gy$	$0.38\ Gy$
Stomach	Mean dose: $8\ Gy$	$6.84\ Gy$	$6.72\ Gy$	$7.08\ Gy$	$6.96\ Gy$

Table 3.4: Patient 1 clinical goals completion table

target coverage is very comparable between the two sets of plans for the static and four-rescan 4D plans, the difference being less than half percent. The dose homogeneity also varies only by a negligible amount for the static and four-rescan 4D plans.

Regarding the conformity of the dose distribution, for the static plans, the conformity of the static spot-reduced plan was slightly better, while for the four-rescan 4D plans, it was the clinical one that was more conformal.

For further evaluation of the fulfillment of the clinical goals prescriptions, static plans together with 4D plans with four rescans were chosen, as the V95 coverage is the most desirable for the four-rescan 4D plan, with the delivery times also being reasonable.

From table 3.4, we can conclude that all four considered plans complete most of the given clinical goals prescriptions with very comparable results. However, all plans fail to complete the clinical goal of a mean dose of 5 Gy for the left lung, while the static spot-reduced plan is the closest with 6.88 Gy. The spot-reduced four-rescan 4D plan fails to complete the $D2\% < 103\%$ clinical goal for the bowel, with 103.7%. The mean dose of 15 Gy prescription for the pancreas is also failed by both static plans. The mean dose of 10 Gy prescription for the left kidney is also failed by both clinical plans, with the spot-reduced plans delivering a dose of 1 Gy less to the organ.
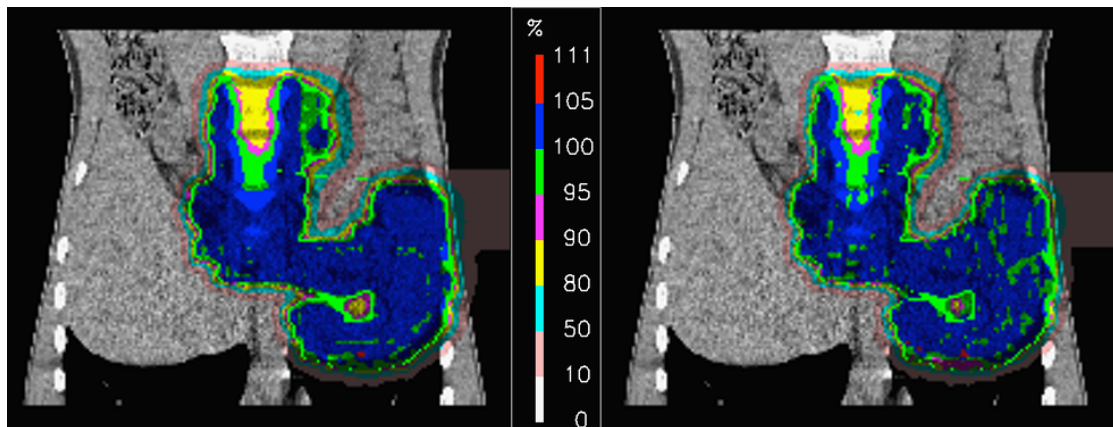

Figure 3.1: Patient 1 dose distribution; *left* - clinical, *right* - spot-reduced

Dose distributions of both static plans can be seen in figure 3.1, with the percentage scale taking as 100 % of the prescribed dose of 20 Gy.

Figure 3.2 shows the cumulative DVH for the PTV structure for this patient, with both sets of plans' DVH curves being nearly identical.
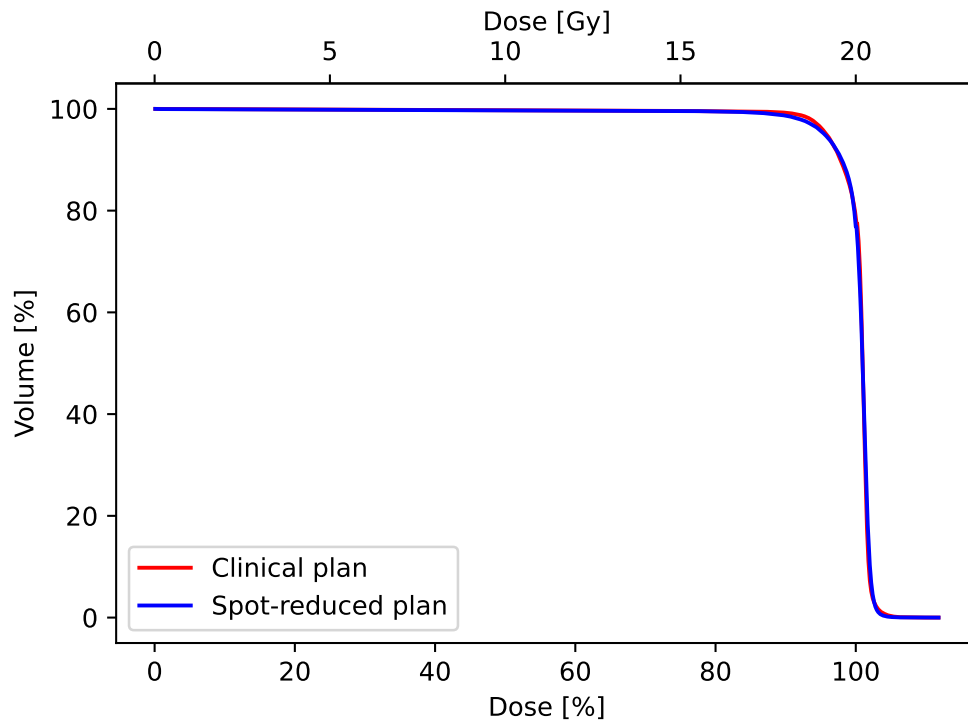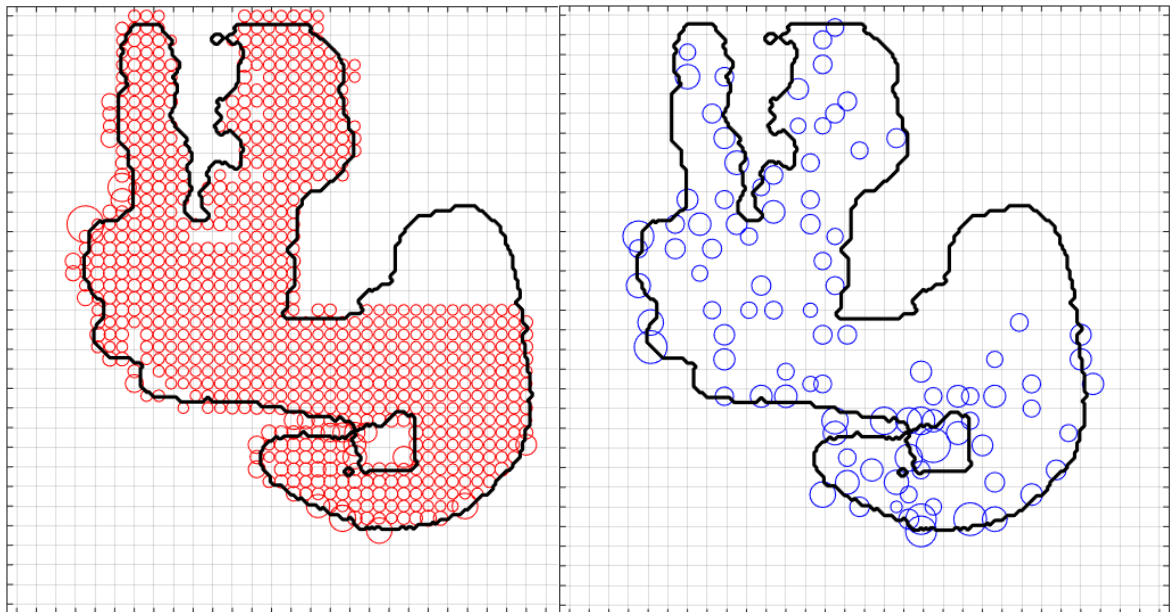
Figure 3.2: Patient 1 PTV DVH static

Figure 3.3: Patient 1 static plans' spot distribution for the field F0, with the energy of 129.2 MeV and the water equivalent thickness of 119.5 mm; *left* - clinical plan, *right* - spot-reduced plan

From figure 3.3, we see that while the clinical plan uses more lower-weighted spots to deliver the dose, the spot-reduced plan uses much fewer high-weighted spots to achieve this goal. This is further confirmed by the energy histogram plot of the spot weights in figure 3.4. A peculiar spot placement pattern can be observed as well. This is most likely due to the fields targeting different sub-regions instead of the entire volume to better take advantage of the 'cross-firing' of the tumor. This open region in the right part of both spot distributions is probably the product of this advantageous targeting by different fields.
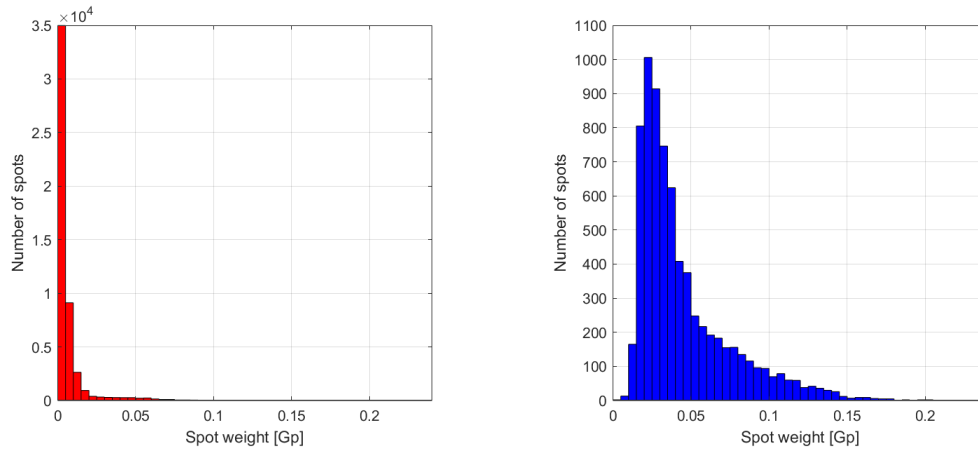

Figure 3.4: Patient 1 spot weight histograms; *left* - clinical plan, *right* - spot-reduced plan

The spot-reduced plan puts more weight on the high-energy spots compared to the clinical plan, as can be seen in figure 3.5, with the most noticeable difference being in the field F1 between 150 and 160 MeV energies.

Figure 3.6 shows the dose-averaged LET distribution, with the values inside the target ranging from 1 to 3 $kev/\mu m$. The highest values can be found towards the liver on the left of the target, with the values ranging from 4 up to 12 $keV/\mu m$.
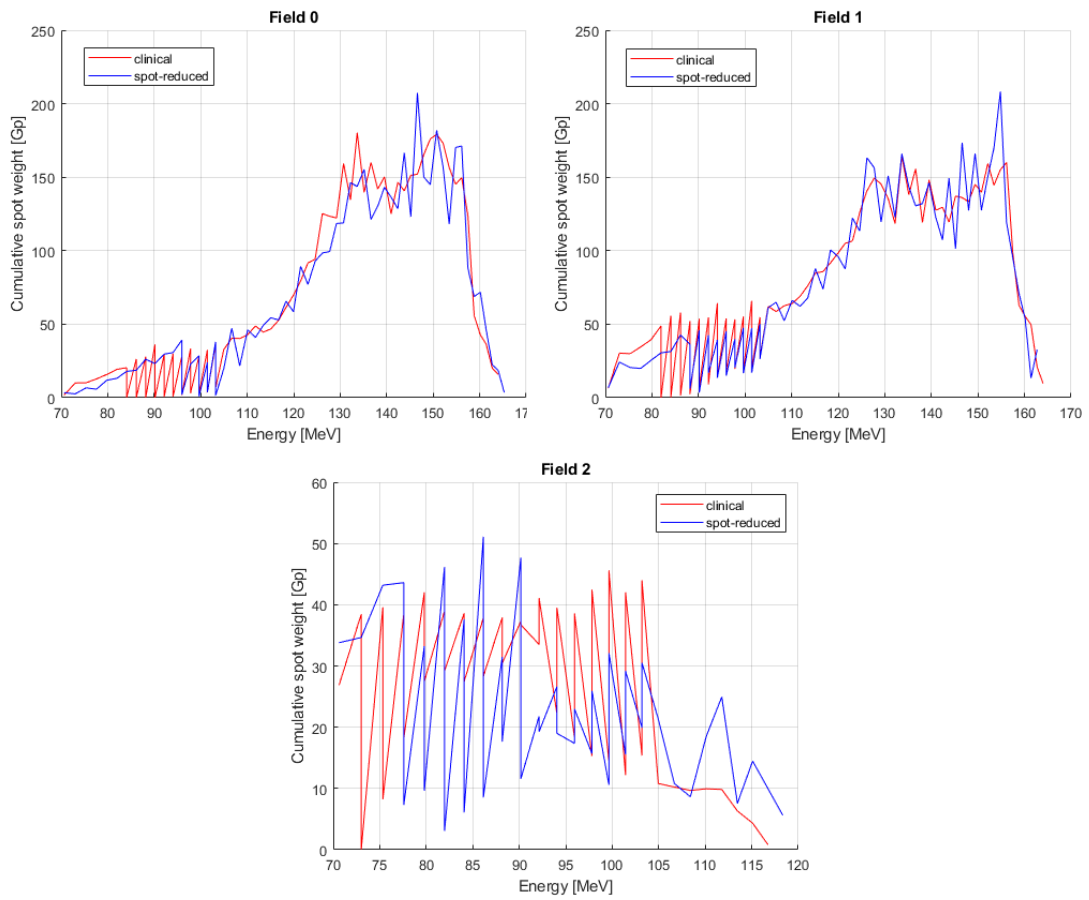
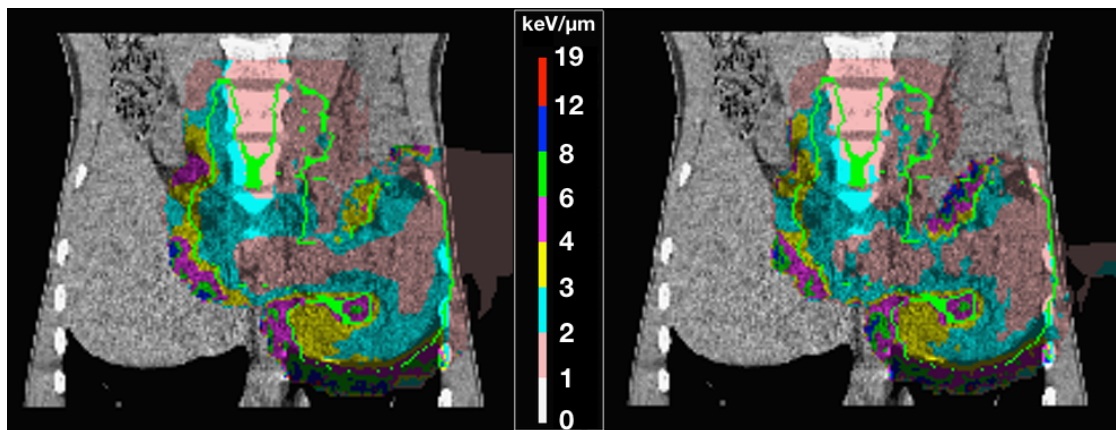Figure 3.5: Patient 1 cumulative spot weight-energy distributions for each field

Figure 3.6: Patient 1 static plans' LET distribution for the PTV; *left* - clinical, *right* - spot-reduced

3.2 Patient 2

Target structure	Main target location	Volume [cm^3]	Prescribed dose [Gy]	Fraction dose [Gy]
PTV_05_1980	Thorax	1801.88	19.8	1.8

Table 3.5: Patient 2 target definition and prescription

This patient was diagnosed with Hodgkin's disease with mixed cellularity. The target is located in the thorax region. The prescribed dose was 19.8 Gy, to be delivered in 11 fractions, with 1.8 Gy being delivered per fraction. The dose was to be delivered in three fields, with the nozzle extensions, angles, and preabsorber settings described in table 3.6.

The PTV volume was 1 801,88 cm^3, with it being located in the lungs and spleen.

Field	Gantry angle [°]	Couch angle [°]	Preabsorber	Nozzle extension [cm]
F0	180	180	AUTO	25
F1	0	180	AUTO	15
F2	-30	180	AUTO	15

Table 3.6: Patient 2 field-specific parameters

For the static plans, the spot reduction achieved was 89.5%. This constitutes a 23.3% reduction in the delivery time or 106.5 s. For the 4D plans, the time reduction was, on average, 28.7% for the spot-reduced plans.

Homogeneity was the best for the static plans, with the *RTOG* index favoring the spot-reduced plan while the *ICRU* index favored the clinical plan. Both homogeneity indices were comparable for the four-rescan 4D plan. For further clinical goals evaluation, only 4D plans with four rescans were chosen.

The custom conformal index indicates that the clinical plans are slightly more conformal than the spot-reduced plans.

As for the completion of the clinical goals, all plans are very much comparable. The biggest difference is for the thyroid, where the spot-reduced plans deliver the dose reduced by more than 1 Gy.

$D_p = 19.8$ Gy	Clinical				Spot-reduced			
	Static	4D			Static	4D		
Number of rescans		**1**	**2**	**4**		**1**	**2**	**4**
Number of spots	60 228				6 322			
Delivery time	457.17 s	457.17 s	636.20 s	995.54 s	350.69 s	350.69 s	452.78 s	657.36 s
Delivery time change					-23.29 %	-23.29 %	-28.83 %	-33.97 %
PTV V95 %	93.64 %	90.44 %	91.69 %	92.26 %	93.55 %	89.70 %	91.87 %	92.11 %
HI$_{RTOG}$	1.18	1.28	1.19	1.26	1.13	1.33	1.26	1.27
HI$_{ICRU}$	0.137	0.222	0.200	0.192	0.152	0.236	0.199	0.199
CI$_{sk}$	0.765	0.738	0.737	0.740	0.754	0.714	0.736	0.736
PTV D2 %	20.71 Gy	21.60 Gy	21.30 Gy	21.21 Gy	20.61 Gy	21.60 Gy	21.09 Gy	21.09
PTV D98 %	17.96 Gy	17.17 Gy	17.31 Gy	17.36 Gy	17.56 Gy	16.87 Gy	17.09 Gy	17.09

Table 3.7: Patient 2 dose metrics and delivery times

OAR	Prescription	Static		4D	
		Clinical	Spot-reduced	Clinical 4 rescans	Spot-reduced 4 rescans
Heart	Mean dose: 5 Gy	8.13 Gy	8.06 Gy	8.24 Gy	8.20 Gy
Breast	Mean dose: 4 Gy	0.56 Gy	0.06 Gy	0.50 Gy	5.94 Gy
Lung L	Mean dose: 10 Gy	7.95 Gy	7.34 Gy	8.59 Gy	7.88 Gy
	Constraint: $V20\,Gy\ <\ 20$ %	3.4 %	3.6 %	8.9 %	6.8 %
	Constraint: $V5\,Gy\ <\ 55$ %	52.2 %	47.5 %	54.4 %	49.6 %
Lung R	Mean dose: 10 Gy	8.78 Gy	8.60 Gy	8.91 Gy	8.71 Gy
	Constraint: $V20\,Gy\ <\ 20$ %	5.3 %	7.2 %	7.5 %	7.5 %
	Constraint: $V5\,Gy\ <\ 55$ %	57.4 %	54.3 %	57.4 %	54.4 %
Thyroid	Mean dose: 20 Gy	11.54 Gy	10.06 Gy	11.86 Gy	10.61 Gy
Spinal cord	Max dose: 30 Gy	20.58 Gy	21.62 Gy	20.81 Gy	21.81 Gy
Esophagus	Max dose: 31 Gy	21.69 Gy	21.44 Gy	21.96 Gy	22.89 Gy
Kidney L	Mean dose: 5 Gy	2.84 Gy	2.79 Gy	2.49 Gy	2.42 Gy
	Max dose: 20 Gy	20.34 Gy	20.60 Gy	20.57 Gy	20.83 Gy
Vertebra	Max dose: 5 Gy	17.98 Gy	17.93 Gy	19.07 Gy	18.97 Gy

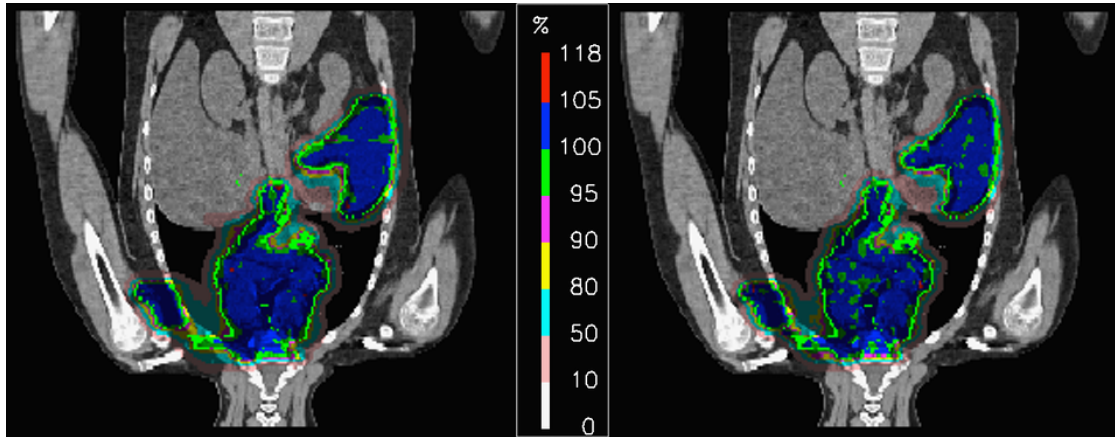Table 3.8: Patient 2 clinical goals completion table

Figure 3.7: Patient 2 dose distribution; *left* - clinical, *right* - spot-reduced
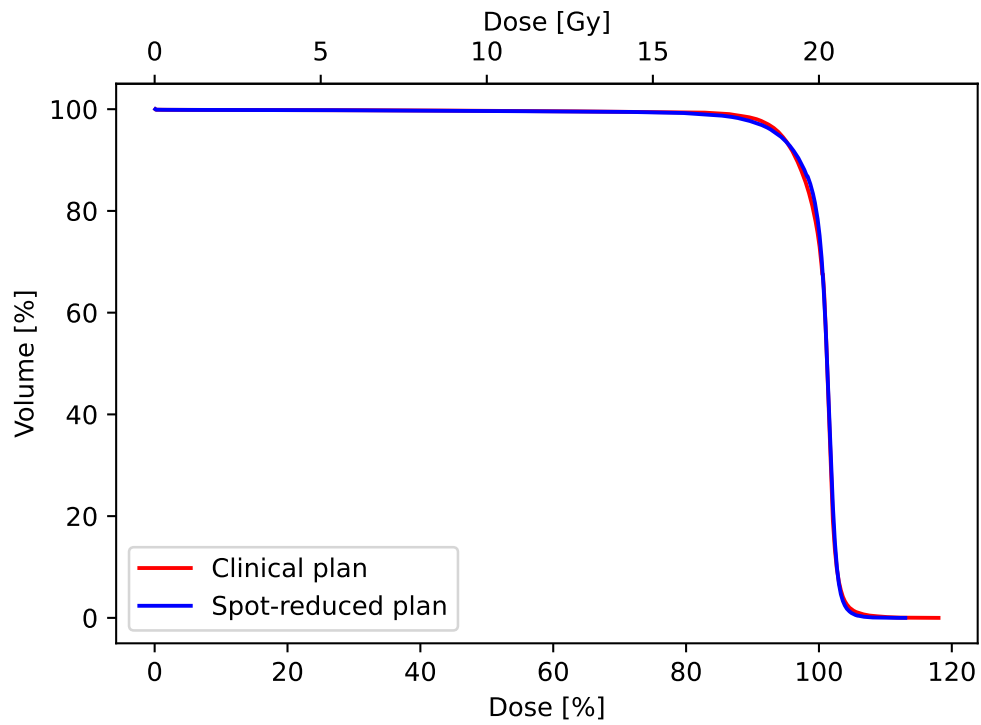

Figure 3.8: Patient 2 PTV DVH static

Dose distributions of both static plans can be seen in figure 3.7, with the percentage scale taking as 100 % of the prescribed dose of 19.8 *Gy*.

From the PTV DVH (figure 3.8), slightly worse conformity of the spot-reduced plan can be observed.
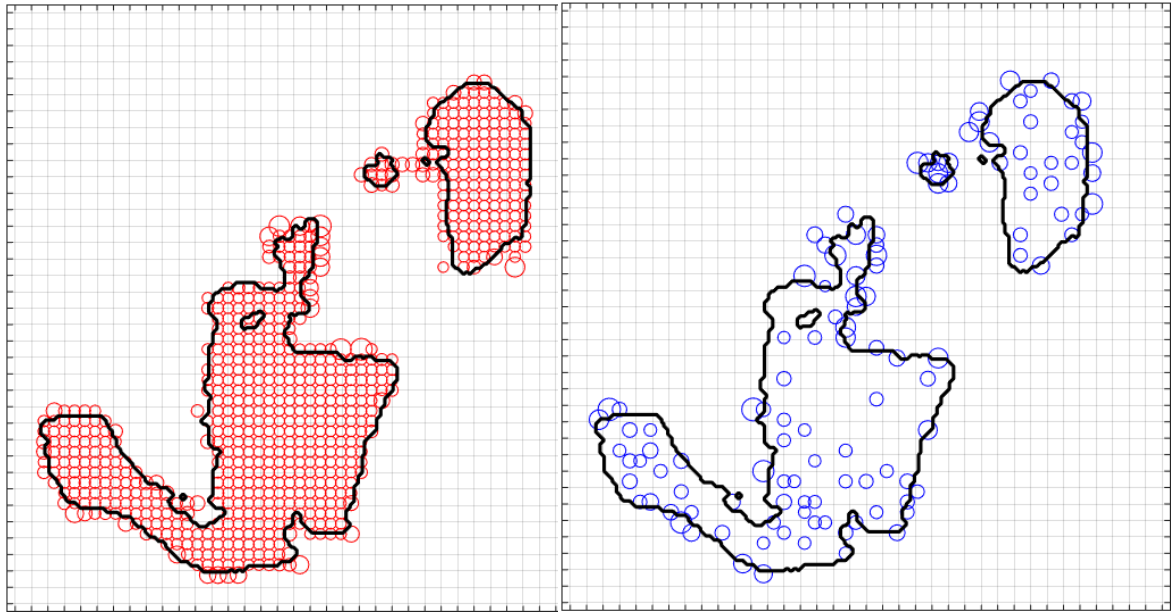
Figure 3.9: Patient 2 static plans' spot distribution for the field F0, with the energy of 124.6 MeV and the water equivalent thickness of 112.1 mm; *left* - clinical plan, *right* - spot-reduced plan

Here (figure 3.9) again, we see that while the clinical plan uses more lower-weighted spots to deliver the dose, the spot-reduced plan uses fewer higher-weighted spots to achieve this goal. Again, this is further confirmed by the histogram visualization of the spot weights in figure 3.10.
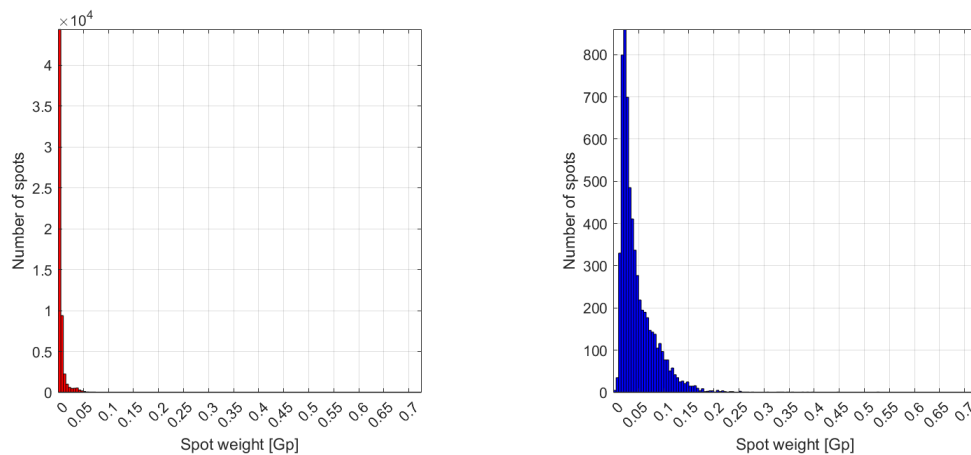

Figure 3.10: Patient 2 spot weight histograms; *left* - clinical plan, *right* - spot-reduced plan
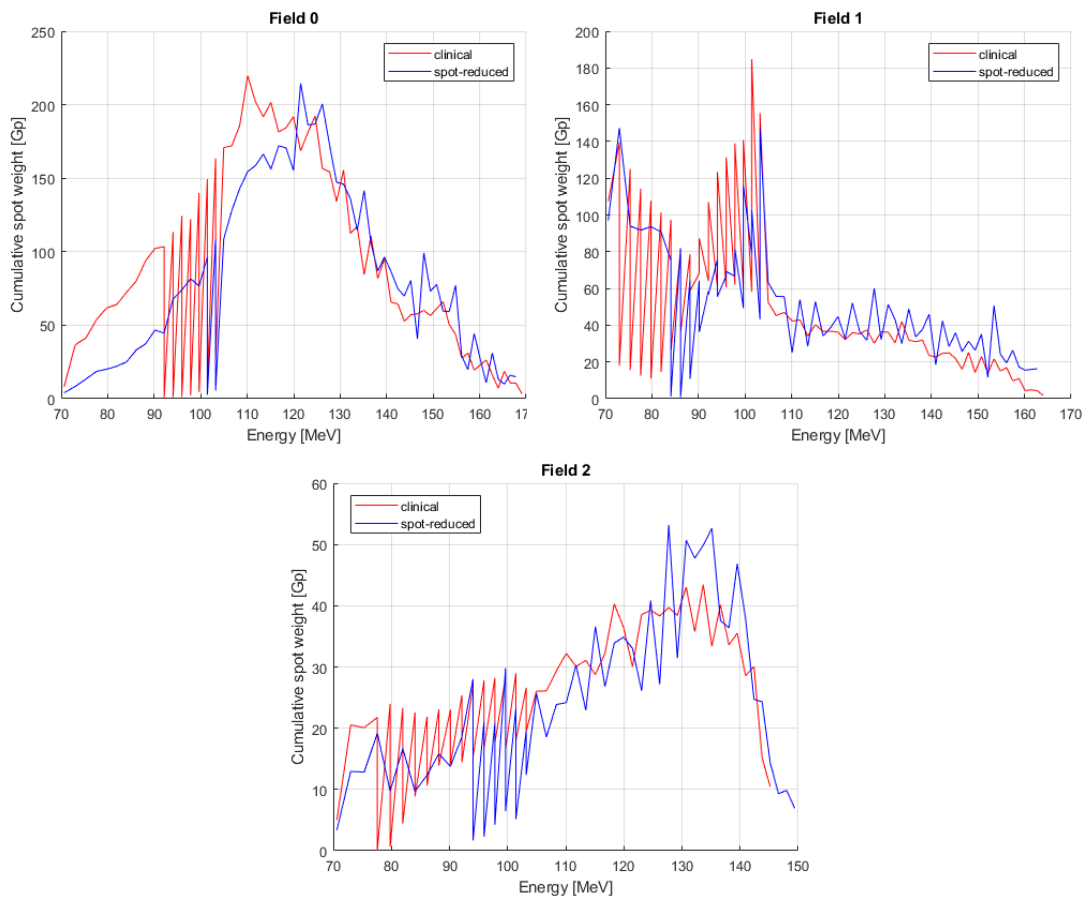
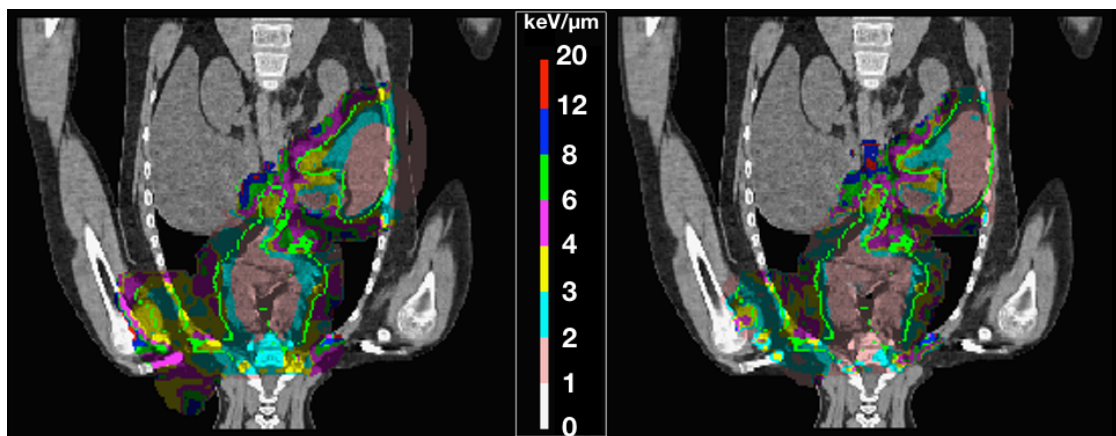Figure 3.11: Patient 2 cumulative spot weight-energy distributions for each field

Figure 3.12: Patient 2 static plans' LET distribution for the PTV; *left* - clinical, *right* - spot-reduced

Focusing on figure 3.11 field F2, we see that, again, near the energy level of 140 MeV, the spot-reduced plan weights the spots much higher than the clinical one does for this energy level.

The LET distribution (figure 3.12) shows that the LET values inside the target range between 1 to 3 $keV/\mu m$, with the spot-reduced plan covering most of the target volume with lower LET values (below 2 $keV/\mu m$) than the clinical one. Higher LET values (up to 12 $keV/\mu m$) can be found outside the target, mostly toward the left side of the target contour.

3.3 Patient 3

Target structure	Main target location	Volume $[cm^3]$	Prescribed dose $[Gy]$	Fraction dose $[Gy]$
PTV_05_1980_MED	Thorax	1683.06	19.8	1.8
PTV_05_1980_LIV	Liver	156.41	19.8	1.8

Table 3.9: Patient 3 target definition and prescription

The patient was diagnosed with mixed cellularity Hodgkin's disease. There is a large mediastinum target defined with a volume of $1\,683{,}06$ cm^3. The treatment was prescribed for 11 fractions, with 1.8 Gy being delivered per fraction, for the total prescribed dose of 19.8 Gy.

This patient also has a second target defined in the liver with a volume of 156,41 cm^3. The dose prescription was the same for this target.

In table 3.10, field-specific parameters can be observed. This patient had the treatment delivered in six fields, this being the highest number of fields among all patients considered in this study.

Field	Gantry angle [°]	Couch angle [°]	Preabsorber	Nozzle extension $[cm]$
F0	0	180	AUTO	25
F1	180	180	AUTO	22
F2	75	180	AUTO	13
F3	30	180	AUTO	22
F4	75	0	AUTO	13
F5	0	180	AUTO	25

Table 3.10: Patient 3 field-specific parameters

The spot reduction achieved was 86.5% for the static plans, which corresponds to a reduction in the delivery time of 20.8%, or 97 s.

Here, however, the V95 coverage suffers. For the liver target, this metric is worse by more than 2% for the static spot-reduced plan. For the 4D plans, however, the V95 coverage of spot-reduced plans is higher on average by more than 5%.

For the mediastinum target, the V95 coverage of spot-reduced plans is better for all plans.

The homogeneity is better by approximately 10% for the *RTOG* index, and for the

$D_p = 19.8$ Gy		**Clinical**				**Spot-reduced**			
		Static	4D			Static	4D		
Number of rescans			1	2	4		1	2	4
Number of spots		54 653				7 359			
Delivery time		564.13 s	564.13 s	773.50 s	1 192.98 s	467.11 s	467.11 s	606.42 s	878.31 s
Delivery time change						-17.20 %	-17.20 %	-21.60 %	-26.38 %
PTV V95 %	LIV	97.95 %	87.79 %	86.50 %	87.75 %	95.25 %	92.86 %	93.72 %	94.37 %
	MED	92.58 %	90.72 %	91.06 %	91.03 %	93.03 %	91.78 %	92.33 %	92.50 %
HI$_{RTOG}$	LIV	1.13	1.26	1.28	1.16	1.01	1.11	1.12	1.08
	MED	1.21	1.22	1.22	1.21	1.11	1.16	1.15	1.11
HI$_{ICRU}$	LIV	0.166	0.267	0.250	0.213	0.127	0.174	0.174	0.140
	MED	0.095	0.195	0.185	0.186	0.175	0.200	0.186	0.182
CI$_{sk}$	LIV	0.316	0.264	0.259	0.274	0.305	0.305	0.296	0.314
	MED	0.843	0.832	0.837	0.835	0.849	0.839	0.844	0.845
PTV D2 %	LIV	20.81 Gy	22.02 Gy	21.78 Gy	21.32 Gy	20.65 Gy	21.17 Gy	21.23 Gy	20.67
	MED	20.71 Gy	21.13 Gy	21.01 Gy	21.03 Gy	20.51 Gy	20.89 Gy	20.69 Gy	20.59
PTV D98 %	LIV	17.48 Gy	16.61 Gy	16.77 Gy	17.05 Gy	18.08 Gy	17.66 Gy	17.70 Gy	17.84
	MED	18.81 Gy	17.23 Gy	17.31 Gy	17.31 Gy	17.01 Gy	16.89 Gy	16.97 Gy	16.95

Table 3.11: Patient 3 dose metrics and delivery times

OAR	Prescription	Static		4D	
		Clinical	Spot-reduced	Clinical 4 rescans	Spot-reduced 4 rescans
Kidney R	Mean dose: 12 Gy	0.16 Gy	0.16 Gy	0.16 Gy	0.17 Gy
Lung L	Mean dose: 15 Gy	2.76 Gy	2.61 Gy	2.80 Gy	2.58 Gy
Lung R	Mean dose: 15 Gy	3.83 Gy	3.72 Gy	3.82 Gy	3.67 Gy
Liver	Mean dose: 15 Gy	3.63 Gy	3.41 Gy	3.63 Gy	3.46 Gy
Thyroid	Mean dose: 20 Gy	19.54 Gy	19.66 Gy	19.59 Gy	19.65 Gy
Heart	Mean dose: 10 Gy	3.21 Gy	3.08 Gy	3.06 Gy	3.19 Gy
Spinal Canal	Constraint: Hotspot < 103 %	110.9 %	104.4 %	109.7 %	104.7 %
Esophagus	Constraint: Hotspot < 103 %	113.8 %	104.4 %	111.5 %	104.5 %

Table 3.12: Patient 3 clinical goals completion table

ICRU index, the results vary by the target in question. For the liver target, the spot-reduced plans are more homogeneous, while for the mediastinum target, the clinical plans are more homogeneous.

The conformity metric for the liver target is, by definition, lower than that of the mediastinum target. The best conformity is achieved for the static plans. For the liver target, it is the static clinical plan that is the most conformal, while for the mediastinum, it is the spot-reduced plan.

For further consideration toward the completion of the clinical goals prescriptions, only static plans and 4D plans with four rescans were considered.

From figure 3.12, we see that the spot-reduced plans fulfill the hotspot constraint much better for esophagus and spinal canal structures. The dose hotspot is better by more than 6% for the bowel structure comparing the static plans.

For the spinal canal structure, the static spot-reduced plan improvement is more than 9%, while for the 4D plan, this improvement decreases to more than 7%.

The rest of the requirements of the clinical goals are completed comparably by all plans.
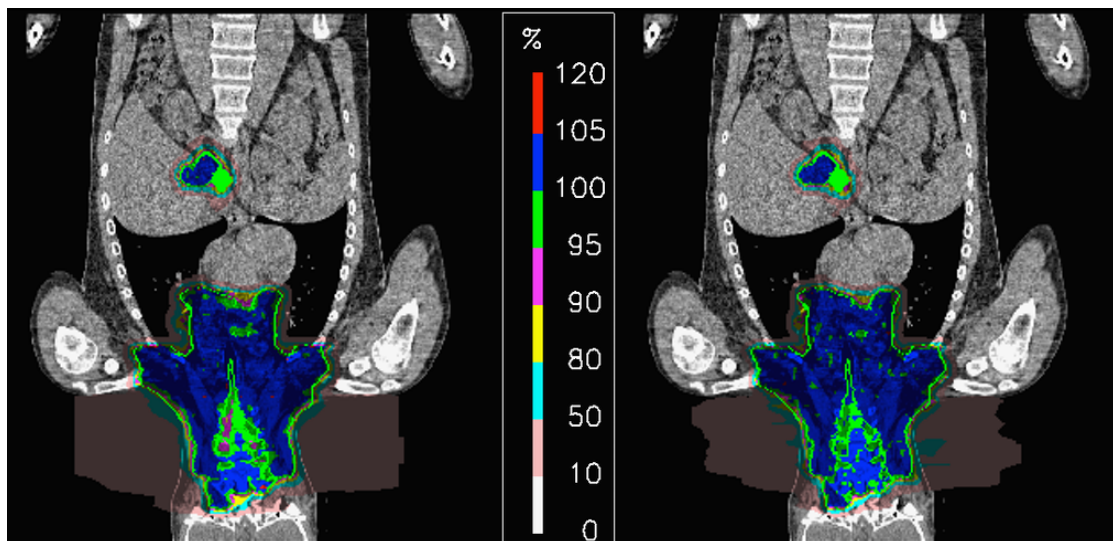

Figure 3.13: Patient 3 dose distribution; *left* - clinical, *right* - spot-reduced

Figure 3.13 shows the dose distribution for the static plans. The percentage scale uses the prescribed dose of 19.8 *Gy* as 100%.

The DVHs were normalized to the mean target dose of the mediastinum target.
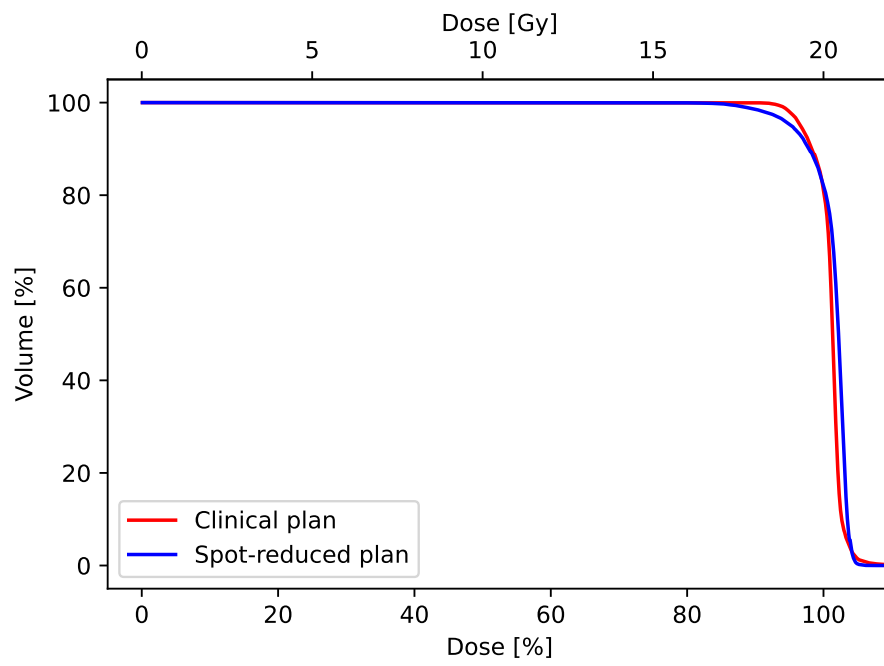
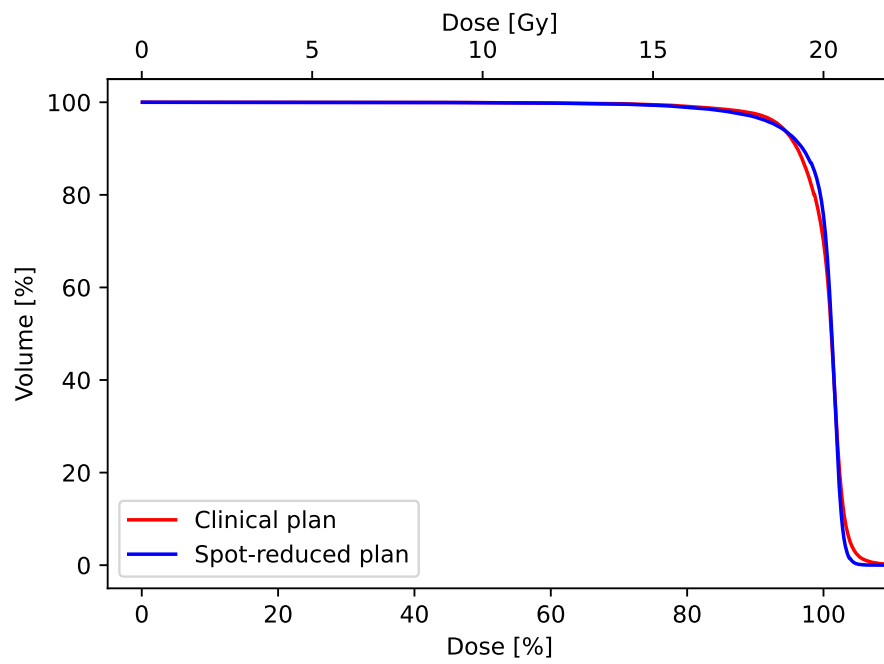Figure 3.14: Patient 3 liver DVH static
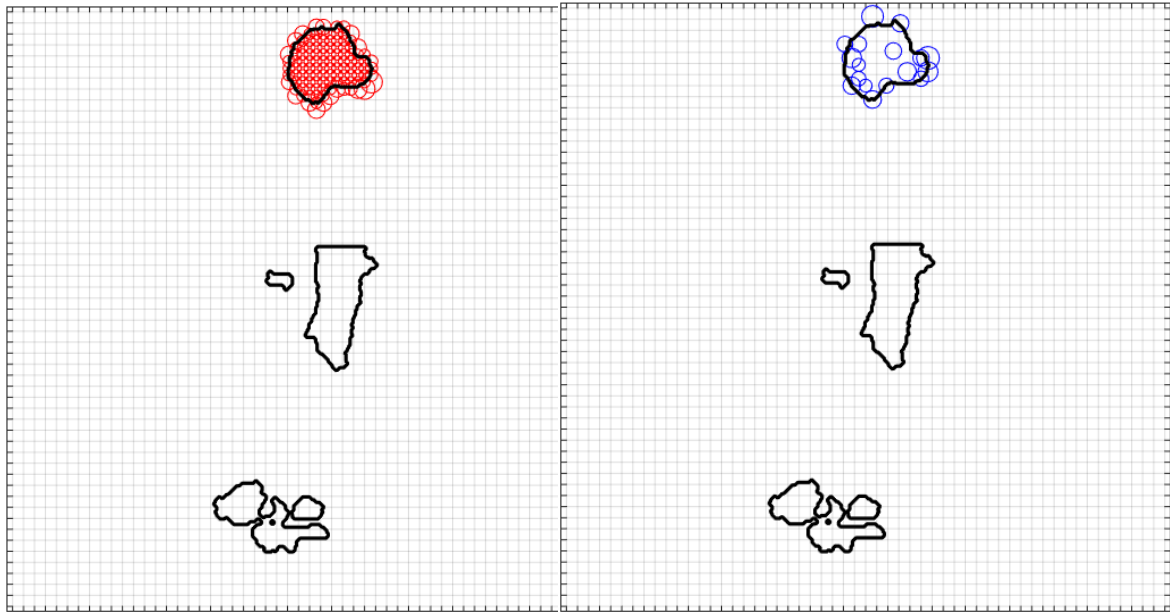

Figure 3.15: Patient 3 mediastinum DVH static

Figure 3.16: Patient 3 liver target static plans' spot distribution for the field F3, with the energy of 124.6 MeV and the water equivalent thickness of 112.1 mm; *left* - clinical plan, *right* - spot-reduced plan.
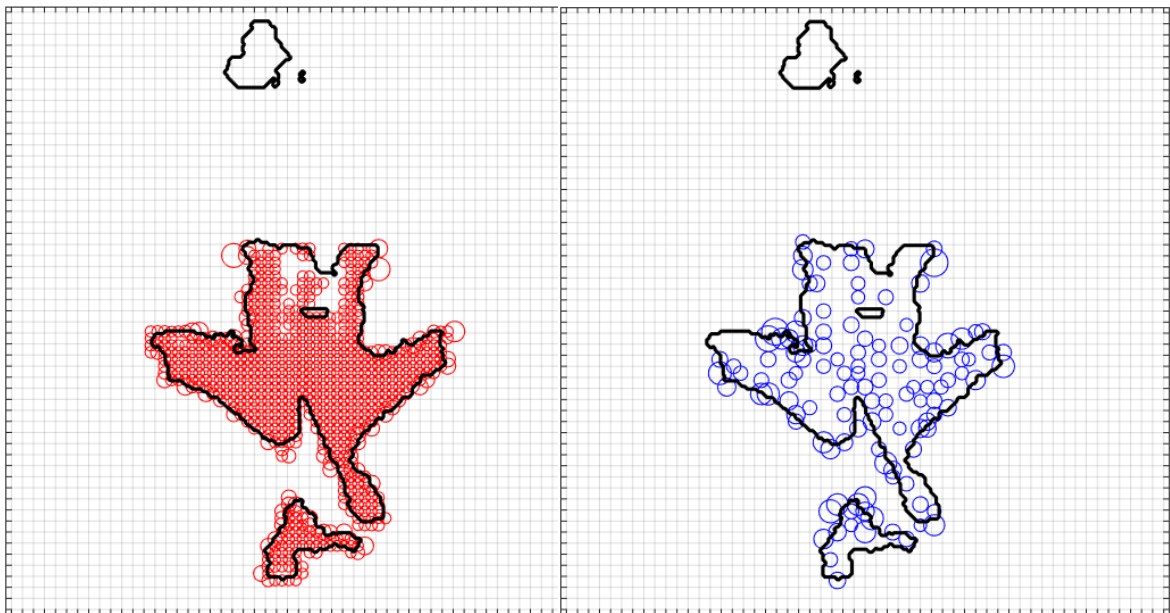

Figure 3.17: Patient 3 mediastinum target static plans' spot distribution for the field F1, with the energy of 124.6 MeV and the water equivalent thickness of 112.1 mm; *left* - clinical plan, *right* - spot-reduced plan.
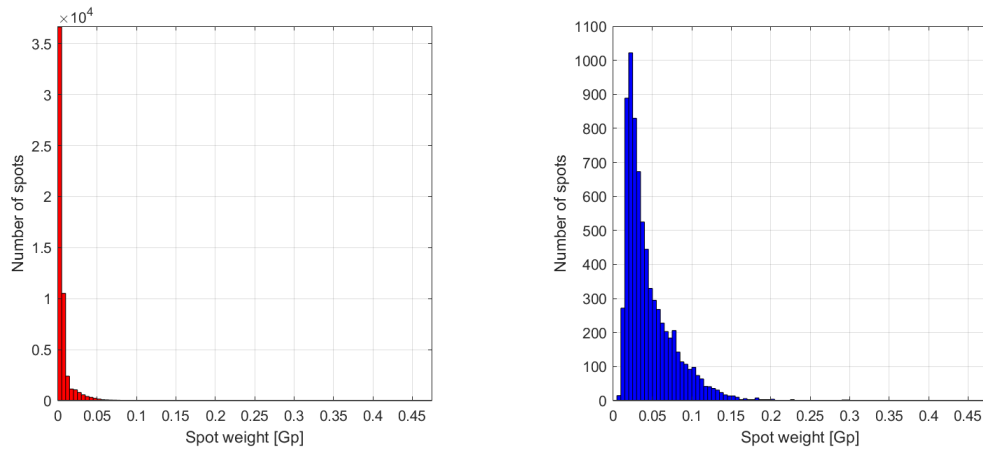
Figure 3.18: Patient 3 spot weight histograms; *left* - clinical plan, *right* - spot-reduced plan
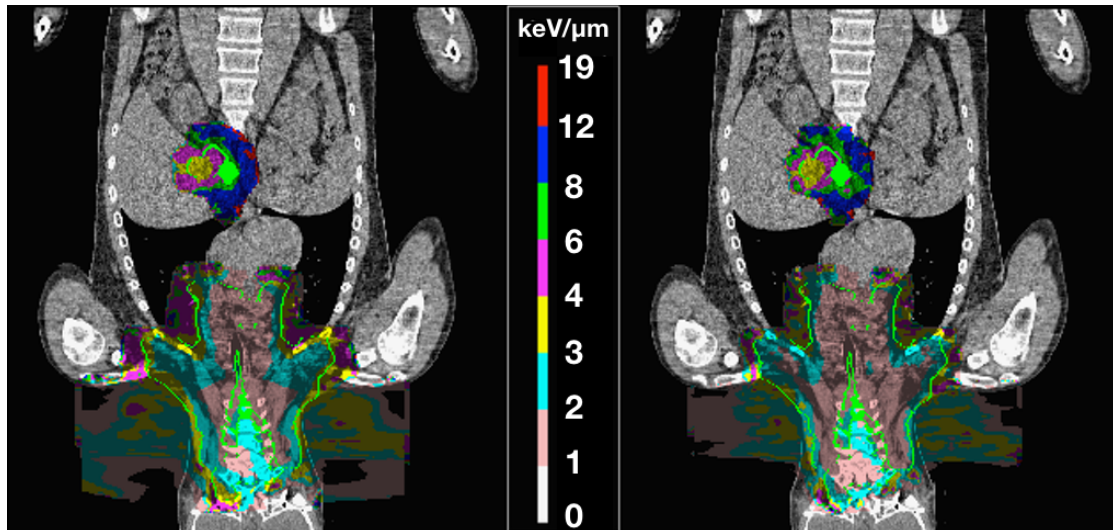

Figure 3.19: Patient 3 static plans' LET distribution for the PTV; *left* - clinical, *right* - spot-reduced

For both targets, the spot-reduced plan delivers the dose with fewer higher-weighted spots compared to more numerous low-weighted spots for the clinical plan (figures 3.16 and 3.17). Again, this phenomenon is more clear in the histogram plot (see 3.18).

Figure 3.19 shows the LET distribution for both of the targets. Here the clinical plan, especially near the liver target, shows more of the increased LET values of up to 12 $keV/\mu m$.

Cumulative spot weight-energy distribution (see 3.20) shows that the spots with higher energy are also the higher-weighted ones, which could have different radiobiological effect.
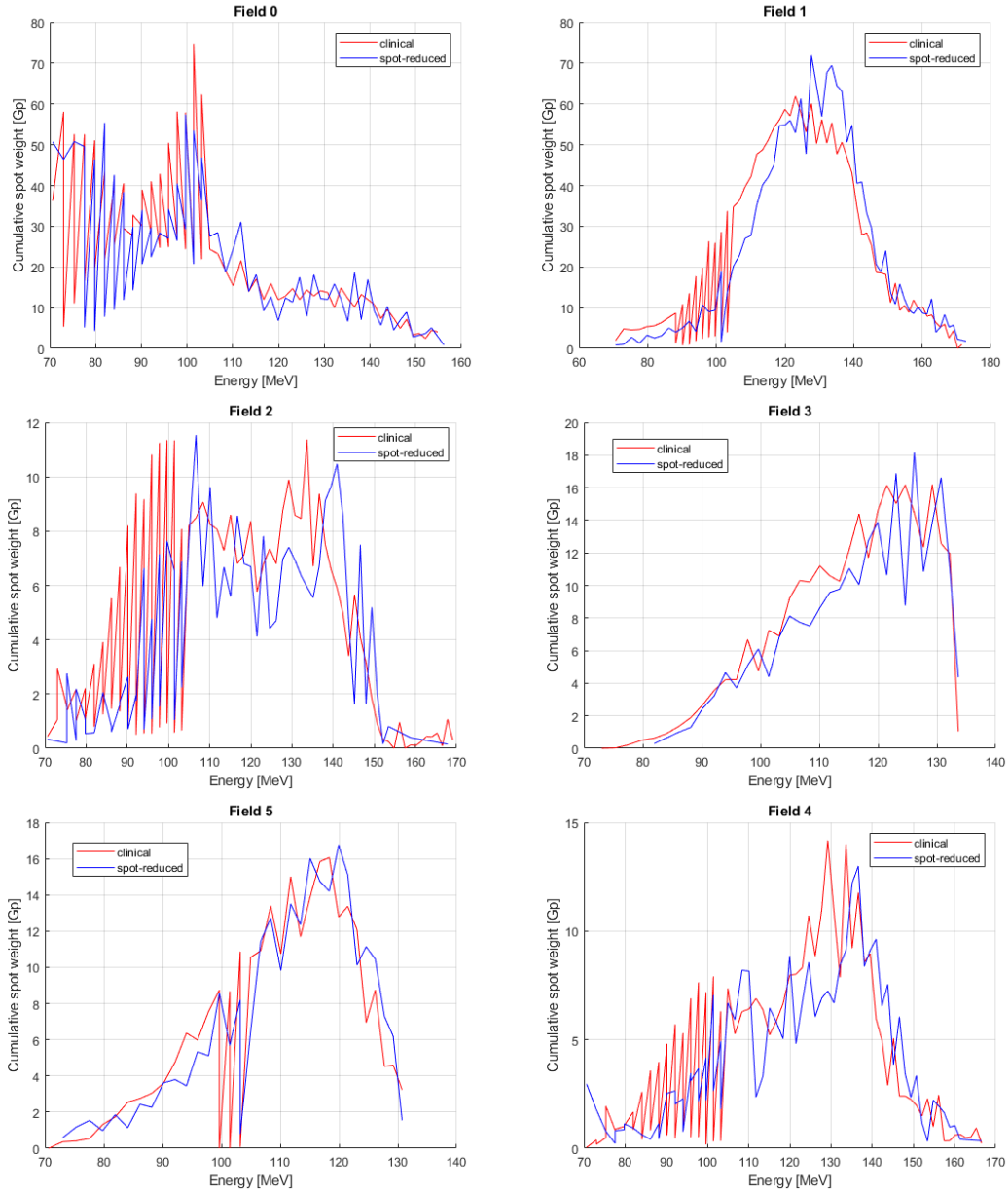

Figure 3.20: Patient 3 cumulative spot weight-energy distributions for each field

3.4   Patient 4

Target structure	Main target location	Volume $[cm^3]$	Prescribed dose $[Gy]$	Fraction dose $[Gy]$
PTV_05_7000	Lung - right	1206.48	70	2

Table 3.13: Patient 4 target definition and prescription

This patient has lung cancer and a target with a volume of $1\,206{,}48$ cm^3. The dose was delivered by four fields in 35 fractions, with the fraction dose being 2 Gy for the total prescription dose of 70 Gy.

The field-specific parameters can be observed in table 3.14.

Field	Gantry angle [°]	Couch angle [°]	Preabsorber	Nozzle extension $[cm]$
F0	-15	180	PREAB_1	15
F1	15	180	PREAB_1	15
F2	165	180	PREAB_1	16
F3	180	180	PREAB_1	20

Table 3.14: Patient 4 field-specific parameters

The V95 coverage of the target structure is better for all the spot-reduced plans. For the static plans, the difference is exactly 1%, while for the 4D plans, this difference decreases.

The spot reduction achieved here was 94.8% comparing the spot-reduced and clinical plans. However, this huge reduction in the number of spots does not correlate with such a huge delivery time reduction. This reduction amounts to 17.6% or 65.9 s for the static plans.

Both homogeneity indices indicate that the spot-reduced plans are more homogeneous than the clinical plans.

As for the conformity of the dose distribution, for static plans, the spot-reduced plan is more conformal than the clinical plan. However, for the four-rescan 4D plan, it is the clinical plan that is the more conformal one.

For the evaluation of the completion of the clinical goals, static plans together with the 4D plans with four rescans were chosen.

Figure 3.16 visualizes the completion of the clinical goals by the chosen plans. Spot-reduced plans provide a considerable improvement in the spine canal, with the dose

$D_p = 70$ Gy	Clinical				Spot-reduced			
	Static	4D			Static	4D		
Number of rescans		**1**	**2**	**4**		**1**	**2**	**4**
Number of spots	33 462				1 751			
Delivery time	375.54 s	375.54 s	508.68 s	774.40 s	309.61 s	309.61 s	392.31 s	559.13 s
Delivery time change					-17.56 %	-17.56 %	-22.88 %	-27.80 %
PTV V95 %	93.32 %	93.02 %	93.05 %	93.32 %	94.32 %	93.51 %	93.68 %	93.76 %
HI$_{RTOG}$	1.21	1.22	1.20	1.20	1.10	1.14	1.14	1.15
HI$_{ICRU}$	0.138	0.170	0.167	0.166	0.125	0.140	0.136	0.135
CI$_{sk}$	0.668	0.665	0.663	0.664	0.670	0.658	0.659	0.660
PTV D2 %	73.85 Gy	74.55 Gy	74.27 Gy	74.20 Gy	72.59 Gy	73.36 Gy	73.15 Gy	73.01
PTV D9 %8	64.12 Gy	62.58 Gy	62.51 Gy	62.51 Gy	63.77 Gy	63.49 Gy	63.56 Gy	63.49

Table 3.15: Patient 4 dose metrics and delivery times

OAR	Prescription	Static		4D	
		Clinical	Spot-reduced	Clinical 4 rescans	Spot-reduced 4 rescans
Spine canal	Max dose: $54\ Gy$	$49.63\ Gy$	$45.50\ Gy$	$56.35\ Gy$	$45.43\ Gy$
	Constraint: $V50\ Gy\ <\ 0.03\ cm^3$	$0.00\ cm^3$	$0.00\ cm^3$	$4.78\ cm^3$	$0.00\ cm^3$
Lungs	Mean dose: $20\ Gy$	$20.86\ Gy$	$20.30\ Gy$	$21.49\ Gy$	$20.86\ Gy$
	Constraint: $V20\ Gy\ <\ 37\ \%$	$37.3\ \%$	$36.2\ \%$	$38.4\ \%$	$37.2\ \%$
	Constraint: $V5\ Gy\ <\ 60\ \%$	$48.5\ \%$	$47.1\ \%$	$49.6\ \%$	$47.9\ \%$
Esophagus	Mean dose: $34\ Gy$	$46.97\ Gy$	$45.92\ Gy$	$46.90\ Gy$	$47.90\ Gy$
	Constraint: $V74\ Gy\ <\ 1\ cm^3$	$0.57\ cm^3$	$0.00\ cm^3$	$0.47\ cm^3$	$0.00\ cm^3$
Brachial plexus	Constraint: $V75\ Gy\ <\ 0.5\ cm^3$	$0.02\ cm^3$	$0.00\ cm^3$	$0.19\ cm^3$	$0.00\ cm^3$
	Constraint: $V74\ Gy\ <\ 1\ cm^3$	$0.17\ cm^3$	$0.00\ cm^3$	$0.11\ cm^3$	$0.00\ cm^3$
	Constraint: $V70\ Gy\ <\ 3\ cm^3$	$2.86\ cm^3$	$1.75\ cm^3$	$2.71\ cm^3$	$1.64\ cm^3$
Heart	Constraint: $V45\ Gy\ <\ 35\ \%$	$4.7\ \%$	$4.6\ \%$	$5.1\ \%$	$5.1\ \%$
	Constraint: $V30\ Gy\ <\ 50\ \%$	$7.0\ \%$	$7.0\ \%$	$7.4\ \%$	$7.4\ \%$
Spinal canal center	Max dose: $50\ Gy$	$45.29\ Gy$	$39.90\ Gy$	$53.41\ Gy$	$40.04\ Gy$

Table 3.16: Patient 4 clinical goals completion table

being lower by up to 13 Gy for the center of the spine canal and comparing the four-rescan 4D plans. The other main difference can be found in the brachial plexus organ. The $V70\ Gy\ <\ 3\ cm^3$ constraint is completed by all considered plans, however, the spot-reduced plans cover a smaller volume by more than 1 cm^3 with the 70 Gy isodose.
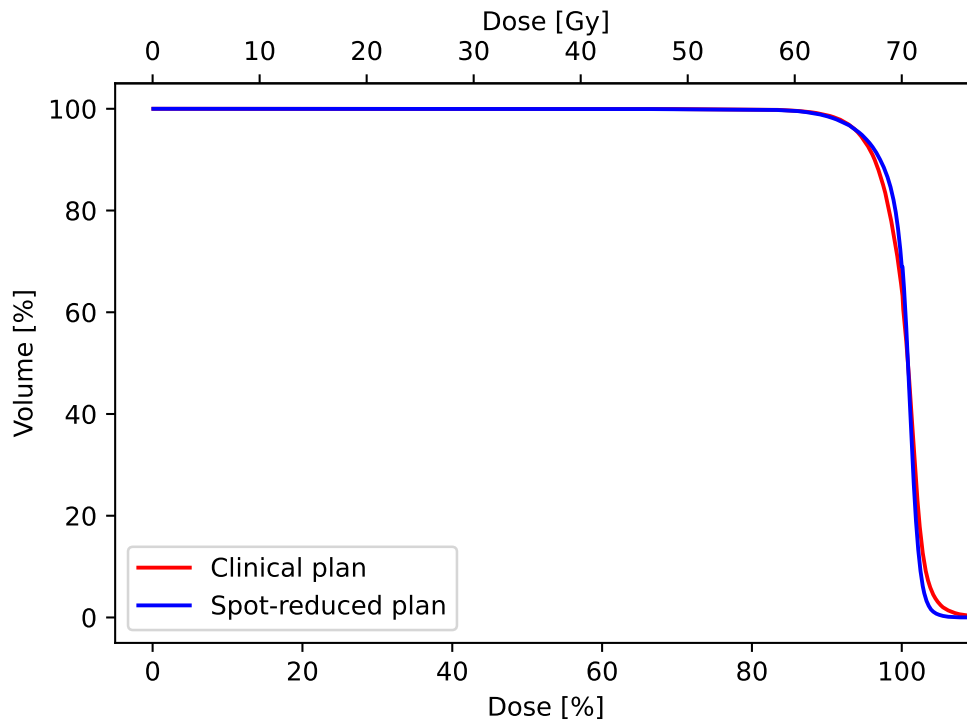
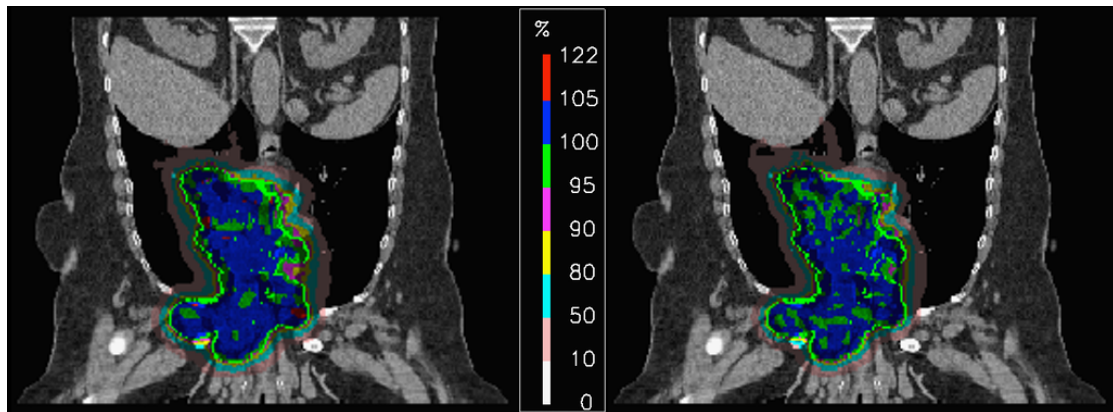

Figure 3.21: Patient 4 PTV DVH static

Figure 3.22: Patient 4 dose distribution; *left* - clinical, *right* - spot-reduced

From the PTV DVH (see 3.21), we can see that the spot-reduced plan is more homogeneous (the decreasing slope is steeper than that of the clinical plan), with it also being more conformal (the more pronounced shoulder).

Figure 3.22 shows the dose distribution for the static plans. The percentage scale uses the prescribed dose of 70 Gy as 100%.
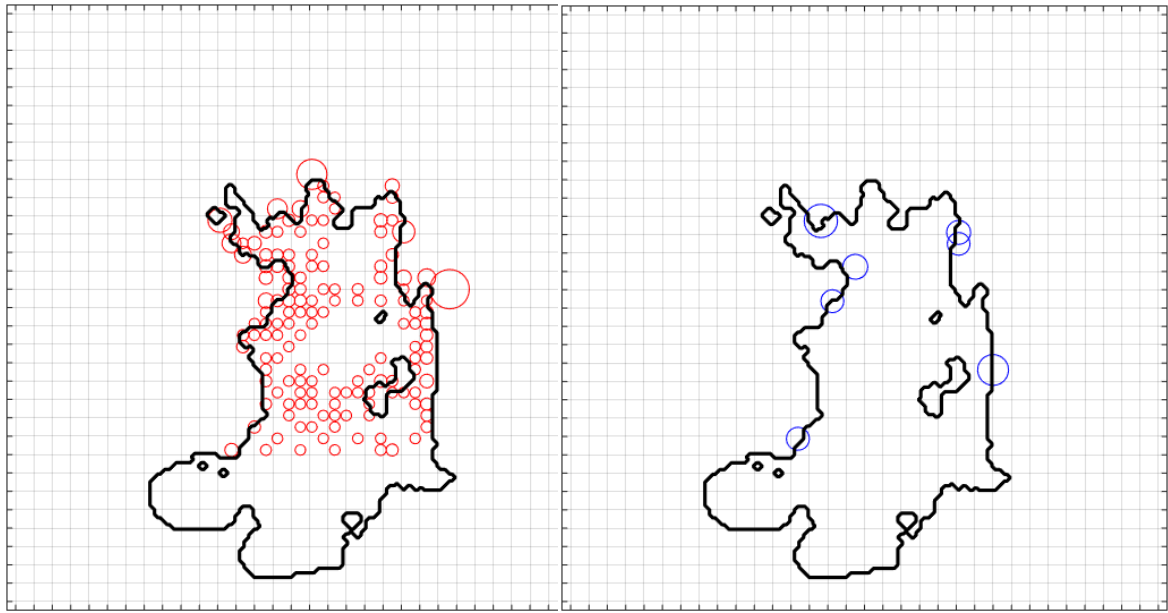
Figure 3.23: Patient 4 static plans' spot distribution for the field F3, with the energy of 150.7 MeV and the water equivalent thickness of 114.9 mm; *left* - clinical plan, *right* - spot-reduced plan

In figure 3.23, we can again see a somewhat interesting spot placement pattern. The most likely explanation is, again, the open region being targeted by a different field to make the most use of 'cross-firing' the target.
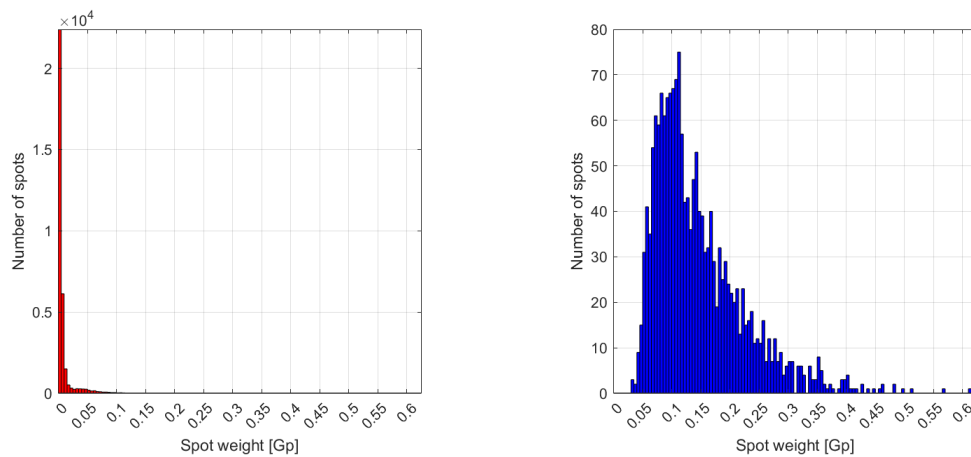

Figure 3.24: Patient 4 spot weight histograms; *left* - clinical plan, *right* - spot-reduced plan
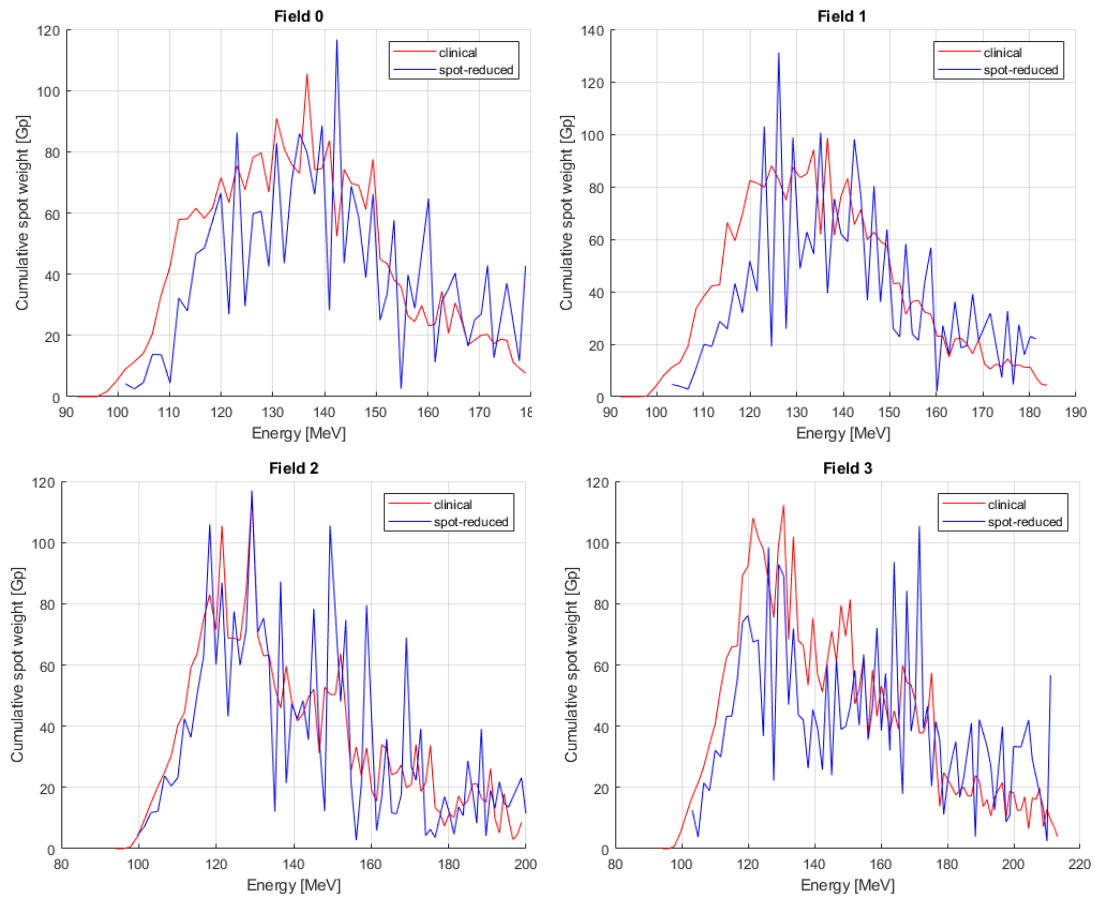
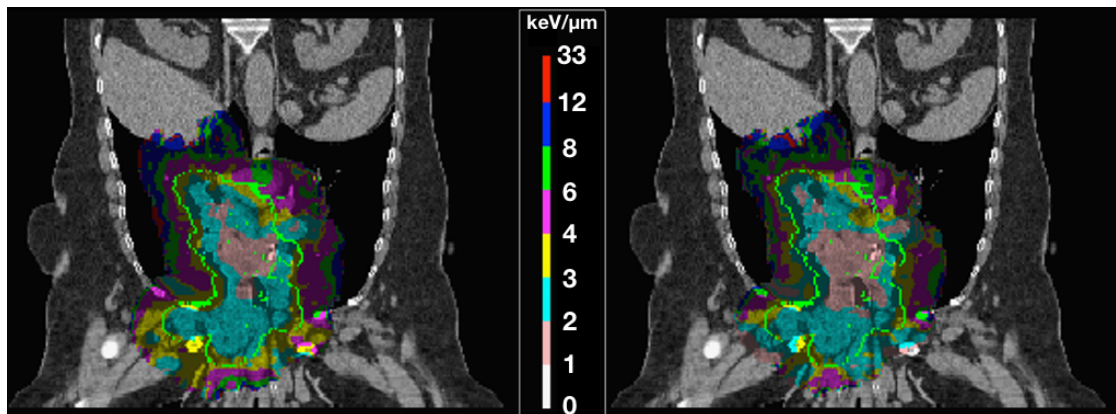Figure 3.25: Patient 4 cumulative spot weight-energy distributions for each field

Figure 3.26: Patient 4 static plans' LET distribution for the PTV; *left* - clinical, *right* - spot-reduced

As for the cumulative spot weight-energy distributions, for field F3, there is a significant difference in the spot weights of higher energy spots. The spot-reduced plan weighting spots with energies between 200 and 220 MeV much more heavily than the clinical plan. The same can be seen in the 160-180 MeV energy range.

The LET distribution for this patient shows again that the average LET value inside the target structure is higher for the clinical plan compared to the spot-reduced plan (see 3.26). Higher LET values (up to 12 $keV/\mu m$) can be found to the left and bottom of the target contour. For the clinical plan, there is a LET hotspot of values up to 33 $keV/\mu m$ inside the right lung (to the left of the target structure in 3.26).

Discussion

In general, the study showed that the huge spot reduction achieved (more than 85 % for all patients' static plans) does not correlate with such a huge reduction in delivery time. For more detail, the total delivery time consists of two main components: beam-on time and dead time.

Spot reduction has an effect on both of these components. As the total number of spots is reduced with the spot reduction algorithm, the total dead time is reduced as well. This is where we can see the most delivery time reduction for the spot-reduced plans. The other component, the beam-on time, increases with the number of monitor units (MU), which is proportional to the weight of a specific spot (i.e., the number of protons). Individual spots in the spot-reduced plans tend to have a higher weight of the spot, and therefore the beam-on time for a single spot is higher for spot-reduced plans. However, the clinical plans need to deliver a higher number of spots, and therefore while the beam-on time for a single spot is lower, the total beam-on time is comparable between the two sets. Usually, for this spot reduction algorithm, the spot-reduced plans are in total composed of 10% fewer protons.

In the majority, the reduction in delivery times was around 20%. The biggest delivery time reduction was found between 4D four-rescan plans for Patient 2. The delivery time was reduced by almost 34%. The percentage of spots that were eliminated by the spot reduction algorithm was around 90% for all patients.

The results show that this spot reduction algorithm can achieve very comparable, if not better, plan quality. When comparing the spot-reduced plans with the plans used for the original patient treatment, the algorithm manages to reduce the delivery time of the dose by a considerable amount. The analysis of energies and cumulative spot weights, LET distributions, and spot placement of both clinical and spot-reduced plans showed that the spot-reduced plans place the higher-weighted spots on the edge of the target, with some of these high-weighted spots transcending the target contour. Spot-reduced plan weights higher spots with higher energies than the clinical plan. The LET distributions slightly favor the spot-reduced plans, with the biggest difference being the high LET hotspot inside the right lung of Patient 4.

In terms of improving the results, the efficiency of lexicographic optimization depends significantly on the planner's experience and knowledge. Therefore, implementing standardization of the input parameters of the spot reduction algorithm, for example, by diagnosis, tumor movement, or size, could greatly improve the comparability of results for different sets of patients.

4.0.1 Alternative delivery time reduction methods

For proton arc therapy, that is, continuous irradiation of the tumor while the gantry rotates, it is necessary for the delivery for a certain angle to be as fast as possible to try to 'match' the gantry's speed of rotation. There are various iterative algorithms used for this purpose that are based on a similar approach as the spot reduction algorithm used in this study. The algorithm called *SPArc*, for example, in each iteration, resamples the spots, adjusts their organization and redistribution, and then also filters the energy layers and resamples them. [31]

Matrix sparsity norm or group sparsity norm optimization (e.g., ℓ_0, ℓ_1, ℓ_2, and ℓ_∞ norms) is a method to filter elements of dose-influence matrices that are part of the optimization process. By applying different types of these sparsity norms and therefore reducing matrix elements, the time needed for inverse dose-influence matrix optimization reduces.

Technically, the ℓ_1-norm optimization is part of spot-reduced planning, as it is the minimization of the total number of protons in the plan.

4.1 Conclusion

This study showed that under certain conditions, the spot reduction approach for large mobile targets could be more efficient in terms of delivery times without necessarily compromising certain plan qualities.

Further studies are needed to evaluate the higher spot weights for higher energies that were seen for the spot-reduced plans and how it relates to the LET distribution presented in this work. If the higher-weighted spots with higher energies are also positioned close to a critical organ, the higher LET values found at the distal edge of such spots could mean relative biological effectiveness of more than 1.1, and the dose delivered by these spots could not be neglected.

Overall this spot reduction algorithm achieves nearly identical, if not better, plan quality while also reducing the delivery time by more than 20 % for all the four-rescan 4D spot-reduced plans, and by more than 14 % for all the static plans. Such results would mean that the implementation of such an algorithm into the clinical practice workflow could be beneficial.

The limitations of these results lie mainly in the two different environments for the (re)optimization of the treatment plans. However, as a basis for further consideration and evaluation of this particular spot reduction algorithm, it is sufficient. To compare the actual delivery times of both sets of plans, instead of comparing estimates, some candidate plans for each patient could be selected and delivered. In the future, more patients could be included in such a study.

A recent study by *Maradia et al., 2022* [32] used the same spot reduction algorithm

to deliver entire fields during a single breath hold ($< 15s$). This study was also done for lung patients, but the PTV volume was significantly lower, with the largest PTV having a volume of 379 cm^3. In this work, the achieved delivery time reduction between clinical and spot-reduced plans was around 40%.

Bibliography

[1] H. Giap and B. Giap, "Historical perspective and evolution of charged particle beam therapy," *Translational Cancer Research*, vol. 1, no. 3, 2012. [Online]. Available: https://tcr.amegroups.com/article/view/595

[2] B. S. Müller and J. J. Wilkens, "Prioritized efficiency optimization for intensity modulated proton therapy," *Physics in Medicine and Biology*, vol. 61, no. 23, pp. 8249–8265, nov 2016. [Online]. Available: https://doi.org/10.1088/0031-9155/61/23/8249

[3] W. D. Newhauser and R. Zhang, "The physics of proton therapy," *Physics in Medicine and Biology*, vol. 60, no. 8, pp. R155–R209, mar 2015. [Online]. Available: https://doi.org/10.1088/0031-9155/60/8/r155

[4] J. Hughes and J. Parsons, "Flash radiotherapy: Current knowledge and future insights using proton-beam therapy," *International journal of molecular sciences*, vol. 21, 09 2020.

[5] Beer, "Bestimmung der absorption des rothen lichts in farbigen flüssigkeiten," *Annalen der Physik*, vol. 162, no. 5, pp. 78–88, 1852. [Online]. Available: https://onlinelibrary.wiley.com/doi/abs/10.1002/andp.18521620505

[6] H. Lin, C. Shi, S. Huang, J. Shen, M. Kang, Q. Chen, H. Zhai, J. McDonough, Z. Tochner, C. Deville, C. B. Simone, and S. Both, "Applications of various range shifters for proton pencil beam scanning radiotherapy," *Radiation Oncology*, vol. 16, no. 1, p. 146, Aug 2021. [Online]. Available: https://doi.org/10.1186/s13014-021-01873-8

[7] M. Goitein, A. J. Lomax, and E. S. Pedroni, "Treating cancer with protons," *Physics Today*, vol. 55, no. 9, pp. 45–50, 2002. [Online]. Available: https://doi.org/10.1063/1.1522215

[8] H. Paganetti, "Proton relative biological effectiveness - uncertainties and opportunities," *Int J Part Ther*, vol. 5, no. 1, pp. 2–14, Sep. 2018.

[9] J. Unkelbach, P. Botas, D. Giantsoudi, B. L. Gorissen, and H. Paganetti, "Re-optimization of intensity modulated proton therapy plans based on linear energy transfer," *Int J Radiat Oncol Biol Phys*, vol. 96, no. 5, pp. 1097–1106, Sep. 2016.

[10] D. Verellen, M. D. Ridder, N. Linthout, K. Tournel, G. Soete, and G. Storme, "Innovations in image-guided radiotherapy," *Nature Reviews Cancer*, vol. 7, no. 12, pp. 949–960, Dec 2007. [Online]. Available: https://doi.org/10.1038/nrc2288

[11] J. H. Phua and K. W. Ang, "Interplay effect in lung cancer proton therapy," *Journal of Xiangya Medicine*, vol. 3, no. 0, 2018. [Online]. Available: https://jxym.amegroups.com/article/view/4883

[12] H. Arimura, Y. Shibayama, M. Haekal, Z. Jin, and K. Ikushima, *Computer-Assisted Target Volume Determination*. Singapore: Springer Singapore, 2017, pp. 87–109. [Online]. Available: https://doi.org/10.1007/978-981-10-2945-5_5

[13] K. Bernatowicz, A. J. Lomax, and A. Knopf, "Comparative study of layered and volumetric rescanning for different scanning speeds of proton beam in liver patients," *Physics in Medicine and Biology*, vol. 58, no. 22, pp. 7905–7920, oct 2013. [Online]. Available: https://doi.org/10.1088/0031-9155/58/22/7905

[14] S. van de Water, M. F. Belosi, F. Albertini, C. Winterhalter, D. C. Weber, and A. J. Lomax, "Shortening delivery times for intensity-modulated proton therapy by reducing the number of proton spots: an experimental verification," *Physics in Medicine &amp Biology*, vol. 65, no. 9, p. 095008, may 2020. [Online]. Available: https://doi.org/10.1088/1361-6560/ab7e7c

[15] S. S. Vedam, P. J. Keall, V. R. Kini, H. Mostafavi, H. P. Shukla, and R. Mohan, "Acquiring a four-dimensional computed tomography dataset using an external respiratory signal," *Physics in Medicine and Biology*, vol. 48, no. 1, pp. 45–62, dec 2002. [Online]. Available: https://doi.org/10.1088/0031-9155/48/1/304

[16] P. Novak, "Identifying the most suitable approach for the treatment of thoracic and abdominal tumors with proton therapy," Master's thesis, ETH, 2020.

[17] P. Keall, "4-dimensional computed tomography imaging and treatment planning," *Seminars in Radiation Oncology*, vol. 14, no. 1, pp. 81–90, 2004, high-Precision Radiation Therapy of Moving Targets. [Online]. Available: https://www.sciencedirect.com/science/article/pii/S1053429603000870

[18] K. Bernatowicz, M. Peroni, R. Perrin, D. C. Weber, and A. Lomax, "Four-dimensional dose reconstruction for scanned proton therapy using liver 4dct-mri," *International Journal of Radiation Oncology, Biology, Physics*, vol. 95, no. 1, pp. 216–223, May 2016. [Online]. Available: https://doi.org/10.1016/j.ijrobp.2016.02.050

[19] A. Lomax, "Intensity modulation methods for proton radiotherapy," *Physics in Medicine and Biology*, vol. 44, no. 1, pp. 185–205, jan 1999. [Online]. Available: https://doi.org/10.1088/0031-9155/44/1/014

[20] A. J. Lomax, T. Böhringer, A. Bolsi, D. Coray, F. Emert, G. Goitein, M. Jermann, S. Lin, E. Pedroni, H. Rutz, O. Stadelmann, B. Timmermann, J. Verwey, and D. C. Weber, "Treatment planning and verification of proton therapy using spot scanning: Initial experiences," *Medical Physics*, vol. 31, no. 11, pp. 3150–3157, 2004. [Online]. Available: https://aapm.onlinelibrary.wiley.com/doi/abs/10.1118/1.1779371

[21] F. Albertini, E. B. Hug, and A. J. Lomax, "The influence of the optimization starting conditions on the robustness of intensity-modulated proton therapy plans," *Physics in Medicine and Biology*, vol. 55, no. 10, pp. 2863–2878, apr 2010. [Online]. Available: https://doi.org/10.1088/0031-9155/55/10/005

[22] E. Rietzel, G. T. Chen, N. C. Choi, and C. G. Willet, "Four-dimensional image-based treatment planning: Target volume segmentation and dose calculation in the presence of respiratory motion," *International Journal of Radiation Oncology, Biology, Physics*, vol. 61, no. 5, pp. 1535–1550, Apr 2005. [Online]. Available: https://doi.org/10.1016/j.ijrobp.2004.11.037

[23] M. Krieger, G. Klimpki, G. Fattori, J. Hrbacek, D. Oxley, S. Safai, D. C. Weber, A. J. Lomax, and Y. Zhang, "Experimental validation of a deforming grid 4d dose calculation for PBS proton therapy," *Physics in Medicine &amp Biology*, vol. 63, no. 5, p. 055005, mar 2018. [Online]. Available: https://doi.org/10.1088/1361-6560/aaad1e

[24] B. Schaffner, E. Pedroni, and A. Lomax, "Dose calculation models for proton treatment planning using a dynamic beam delivery system: an attempt to include density heterogeneity effects in the analytical dose calculation," *Physics in Medicine and Biology*, vol. 44, no. 1, pp. 27–41, jan 1999. [Online]. Available: https://doi.org/10.1088/0031-9155/44/1/004

[25] R. E. Drzymala, R. Mohan, L. Brewster, J. Chu, M. Goitein, W. Harms, and M. Urie, "Dose-volume histograms," *International Journal of Radiation Oncology, Biology, Physics*, vol. 21, no. 1, pp. 71–78, May 1991. [Online]. Available: https://doi.org/10.1016/0360-3016(91)90168-4

[26] L. P. Kaplan and S. S. Korreman, "A systematically compiled set of quantitative metrics to describe spatial characteristics of radiotherapy dose distributions and aid in treatment planning," *Physica Medica*, vol. 90, pp. 164–175, 2021. [Online]. Available: https://www.sciencedirect.com/science/article/pii/S1120179721003136

[27] E. Shaw, R. Kline, M. Gillin, L. Souhami, A. Hirschfeld, R. Dinapoli, and L. Martin, "Radiation therapy oncology group: Radiosurgery quality assurance guidelines," *International Journal of Radiation Oncology*Biology*Physics*, vol. 27, no. 5, pp. 1231–1239, 1993. [Online]. Available: https://www.sciencedirect.com/science/article/pii/036030169390548A

[28] Q. Wu, R. Mohan, M. Morris, A. Lauve, and R. Schmidt-Ullrich, "Simultaneous integrated boost intensity-modulated radiotherapy for locally advanced head-and-neck squamous cell carcinomas. i: dosimetric results," *International Journal of Radiation Oncology, Biology, Physics*, vol. 56, no. 2, pp. 573–585, Jun 2003. [Online]. Available: https://doi.org/10.1016/S0360-3016(02)04617-5

[29] T. Kataria, K. Sharma, V. Subramani, K. P. Karrthick, and S. S. Bisht, "Homogeneity index: An objective tool for assessment of conformal radiation treatments," *J Med Phys*, vol. 37, no. 4, pp. 207–213, Oct. 2012.

[30] "International commission on radiation units and measurements," *J ICRU*, vol. 14, no. 1, p. NP, Apr. 2014.

[31] G. Liu, X. Li, L. Zhao, W. Zheng, A. Qin, S. Zhang, C. Stevens, D. Yan, P. Kabolizadeh, and X. Ding, "A novel energy sequence optimization algorithm for efficient spot-scanning proton arc (sparc) treatment delivery," *Acta Oncologica*, vol. 59, no. 10, pp. 1178–1185, 2020, pMID: 32421375. [Online]. Available: https://doi.org/10.1080/0284186X.2020.1765415

[32] V. Maradia, S. van de Water, D. Meer, D. C. Weber, A. J. Lomax, and S. Psoroulas, "Ultra-fast pencil beam scanning proton therapy for locally advanced non-small-cell lung cancers: Field delivery within a single breath-hold," *Radiotherapy and Oncology*, vol. 174, pp. 23–29, Sep 2022. [Online]. Available: https://doi.org/10.1016/j.radonc.2022.06.018